Monthly Notices of the ROYAL ASTRONOMICAL SOCIETY

Mon. Not. R. Astron. Soc. **424,** 1614–1635 (2012) doi:10.1111/j.1365-2966.2012.20912.x

The *Herschel*★ Multi-tiered Extragalactic Survey: HerMES

S. J. Oliver,[1]† J. Bock,[2,3] B. Altieri,[4] A. Amblard,[5] V. Arumugam,[6] H. Aussel,[7] T. Babbedge,[8] A. Beelen,[9] M. Béthermin,[7,9] A. Blain,[2] A. Boselli,[10] C. Bridge,[2] D. Brisbin,[11] V. Buat,[10] D. Burgarella,[10] N. Castro-Rodríguez,[12,13] A. Cava,[14] P. Chanial,[7] M. Cirasuolo,[15] D. L. Clements,[8] A. Conley,[16] L. Conversi,[4] A. Cooray,[2,17] C. D. Dowell,[2,3] E. N. Dubois,[1] E. Dwek,[18] S. Dye,[19] S. Eales,[20] D. Elbaz,[7] D. Farrah,[1] A. Feltre,[21] P. Ferrero,[12,13] N. Fiolet,[9,22] M. Fox,[8] A. Franceschini,[21] W. Gear,[20] E. Giovannoli,[10] J. Glenn,[16,23] Y. Gong,[17] E. A. González Solares,[24] M. Griffin,[20] M. Halpern,[25] M. Harwit,[26] E. Hatziminaoglou,[27] S. Heinis,[10] P. Hurley,[1] H. S. Hwang,[7] A. Hyde,[8] E. Ibar,[15] O. Ilbert,[10] K. Isaak,[28] R. J. Ivison,[6,15] G. Lagache,[9] E. Le Floc'h,[7] L. Levenson,[2,3] B. Lo Faro,[21] N. Lu,[2,29] S. Madden,[7] B. Maffei,[30] G. Magdis,[7] G. Mainetti,[21] L. Marchetti,[21] G. Marsden,[25] J. Marshall,[2,3] A. M. J. Mortier,[8] H. T. Nguyen,[2,3] B. O'Halloran,[8] A. Omont,[22] M. J. Page,[31] P. Panuzzo,[7] A. Papageorgiou,[20] H. Patel,[8] C. P. Pearson,[32,33] I. Pérez-Fournon,[12,13] M. Pohlen,[20] J. I. Rawlings,[31] G. Raymond,[20] D. Rigopoulou,[32,34] L. Riguccini,[7] D. Rizzo,[8] G. Rodighiero,[21] I. G. Roseboom,[1,6] M. Rowan-Robinson,[8] M. Sánchez Portal,[4] B. Schulz,[2,29] Douglas Scott,[25] N. Seymour,[31,35] D. L. Shupe,[2,29] A. J. Smith,[1] J. A. Stevens,[36] M. Symeonidis,[31] M. Trichas,[37] K. E. Tugwell,[31] M. Vaccari,[21] I. Valtchanov,[4] J. D. Vieira,[2] M. Viero,[2] L. Vigroux,[22] L. Wang,[1] R. Ward,[1] J. Wardlow,[17] G. Wright,[15] C. K. Xu[2,29] and M. Zemcov[2,3]

[1]*Astronomy Centre, Department of Physics and Astronomy, University of Sussex, Brighton BN1 9QH*
[2]*California Institute of Technology, 1200 E. California Boulevard, Pasadena, CA 91125, USA*
[3]*Jet Propulsion Laboratory, 4800 Oak Grove Drive, Pasadena, CA 91109, USA*
[4]*Herschel Science Centre, European Space Astronomy Centre, Villanueva de la Cañada, 28691 Madrid, Spain*
[5]*NASA, Ames Research Center, Moffett Field, CA 94035, USA*
[6]*Institute for Astronomy, University of Edinburgh, Royal Observatory, Blackford Hill, Edinburgh EH9 3HJ*
[7]*Laboratoire AIM-Paris-Saclay, CEA/DSM/Irfu – CNRS – Université Paris Diderot, CE-Saclay, pt courrier 131, F-91191 Gif-sur-Yvette, France*
[8]*Astrophysics Group, Imperial College London, Blackett Laboratory, Prince Consort Road, London SW7 2AZ*
[9]*Institut d'Astrophysique Spatiale (IAS), bâtiment 121, Université Paris-Sud 11 and CNRS (UMR 8617), 91405 Orsay, France*
[10]*Laboratoire d'Astrophysique de Marseille, OAMP, Université Aix-marseille, CNRS, 38 rue Frédéric Joliot-Curie, 13388 Marseille Cedex 13, France*
[11]*Department of Astronomy, Space Science Building, Cornell University, Ithaca, NY 14853-6801, USA*
[12]*Instituto de Astrofísica de Canarias (IAC), E-38200 La Laguna, Tenerife, Spain*
[13]*Departamento de Astrofísica, Universidad de La Laguna (ULL), E-38205 La Laguna, Tenerife, Spain*
[14]*Departamento de Astrofísica, Facultad de CC. Físicas, Universidad Complutense de Madrid, E-28040 Madrid, Spain*
[15]*UK Astronomy Technology Centre, Royal Observatory, Blackford Hill, Edinburgh EH9 3HJ*
[16]*Center for Astrophysics and Space Astronomy, University of Colorado, 389 UCB, Boulder, CO 80309, USA*
[17]*Department of Physics and Astronomy, University of California, Irvine, CA 92697, USA*
[18]*Observational Cosmology Lab, Code 665, NASA Goddard Space Flight Center, Greenbelt, MD 20771, USA*
[19]*School of Physics and Astronomy, University of Nottingham, Nottingham NG7 2RD*
[20]*School of Physics and Astronomy, Cardiff University, Queens Buildings, The Parade, Cardiff CF24 3AA*
[21]*Dipartimento di Astronomia, Università di Padova, vicolo Osservatorio, 3, 35122 Padova, Italy*
[22]*Institut d'Astrophysique de Paris, UMR 7095, CNRS, UPMC Univ. Paris 06, 98bis boulevard Arago, F-75014 Paris, France*
[23]*Department of Astrophysical and Planetary Sciences, CASA 389-UCB, University of Colorado, Boulder, CO 80309, USA*
[24]*Institute of Astronomy, University of Cambridge, Madingley Road, Cambridge CB3 0HA*

★*Herschel* is an ESA space observatory with science instruments provided by European-led Principal Investigator consortia and with important participation from NASA.

†E-mail: S.Oliver@Sussex.ac.uk

© 2012 The Authors
Monthly Notices of the Royal Astronomical Society © 2012 RAS

Downloaded from http://mnras.oxfordjournals.org/ at NASA Goddard Space Flight Ctr on July 14, 2014

[25]*Department of Physics & Astronomy, University of British Columbia, 6224 Agricultural Road, Vancouver, BC V6T 1Z1, Canada*
[26]*511 H Street, SW, Washington, DC 20024-2725, USA*
[27]*ESO, Karl-Schwarzschild-Str. 2, 85748 Garching bei München, Germany*
[28]*ESA Research and Scientific Support Department, ESTEC/SRE-SA, Keplerlaan 1, 2201 AZ Noordwijk, the Netherlands*
[29]*Infrared Processing and Analysis Center, MS 100-22, California Institute of Technology, JPL, Pasadena, CA 91125, USA*
[30]*School of Physics and Astronomy, The University of Manchester, Alan Turing Building, Oxford Road, Manchester M13 9PL*
[31]*Mullard Space Science Laboratory, University College London, Holmbury St. Mary, Dorking, Surrey RH5 6NT*
[32]*RAL Space, Rutherford Appleton Laboratory, Chilton, Didcot, Oxfordshire OX11 0QX*
[33]*Institute for Space Imaging Science, University of Lethbridge, Lethbridge, AB T1K 3M4, Canada*
[34]*Department of Astrophysics, Denys Wilkinson Building, University of Oxford, Keble Road, Oxford OX1 3RH*
[35]*CSIRO Astronomy & Space Science, PO Box 76, Epping, NSW 1710, Australia*
[36]*Centre for Astrophysics Research, University of Hertfordshire, College Lane, Hatfield, Hertfordshire AL10 9AB*
[37]*Harvard–Smithsonian Center for Astrophysics, 60 Garden Street, Cambridge, MA 02138, USA*

Accepted 2012 March 12. Received 2012 January 5; in original form 2011 July 20

ABSTRACT

The *Herschel* Multi-tiered Extragalactic Survey (HerMES) is a legacy programme designed to map a set of nested fields totalling ∼380 deg^2. Fields range in size from 0.01 to ∼20 deg^2, using the *Herschel*-Spectral and Photometric Imaging Receiver (SPIRE) (at 250, 350 and 500 μm) and the *Herschel*-Photodetector Array Camera and Spectrometer (PACS) (at 100 and 160 μm), with an additional wider component of 270 deg^2 with SPIRE alone. These bands cover the peak of the redshifted thermal spectral energy distribution from interstellar dust and thus capture the reprocessed optical and ultraviolet radiation from star formation that has been absorbed by dust, and are critical for forming a complete multiwavelength understanding of galaxy formation and evolution.

The survey will detect of the order of 100 000 galaxies at 5σ in some of the best-studied fields in the sky. Additionally, HerMES is closely coordinated with the PACS Evolutionary Probe survey. Making maximum use of the full spectrum of ancillary data, from radio to X-ray wavelengths, it is designed to facilitate redshift determination, rapidly identify unusual objects and understand the relationships between thermal emission from dust and other processes. Scientific questions HerMES will be used to answer include the total infrared emission of galaxies, the evolution of the luminosity function, the clustering properties of dusty galaxies and the properties of populations of galaxies which lie below the confusion limit through lensing and statistical techniques.

This paper defines the survey observations and data products, outlines the primary scientific goals of the HerMES team, and reviews some of the early results.

Key words: surveys – galaxies: evolution – infrared: galaxies – submillimetre: galaxies.

1 INTRODUCTION AND SCIENCE GOALS

Understanding how galaxies form and evolve over cosmological time is a key goal in astrophysics. Over the last decade, our understanding of the background cosmology has improved to such an extent (e.g. Spergel et al. 2003) that we think we have a reasonable understanding of the formation of structure in the underlying dark matter distribution (e.g. Springel, Frenk & White 2006). However, galaxy formation and evolution are driven by dissipative, non-linear processes within the potential wells of virialized dark matter haloes which are much more complex physical processes which have defied full modelling. Observations play a critical role in constraining models of galaxy formation, the evolution of star formation activity and the various roles played by galaxy stellar mass, dark matter halo mass and environment.

The central importance of far-infrared (FIR) and submillimetre (submm) observations becomes clear when one realizes that the approximately half of all the luminous power (Puget et al. 1996; Fixsen et al. 1998; Lagache, Puget & Gispert 1999) which makes up the extragalactic background radiation – power which originated from stars and active galactic nuclei (AGN) – was emitted at optical/ultraviolet wavelengths, absorbed by dust, and reradiated in the FIR/submm. To form a complete picture of the evolution of galaxies, the optical regime alone cannot be used to fully trace the activity (e.g. the brightest submm galaxy in the *Hubble Deep Field* is not even detected in the optical; Dunlop et al. 2004). Furthermore, submm observations provide a bridge in both wavelength and redshift between the $z > 2$ Universe, primarily probed on the Rayleigh–Jeans side of the spectral energy distribution (SED) by ground-based submm telescopes, and the lower-z Universe, sampled on the Wein side of the SED by *Spitzer*.

FIR/submm luminosity is thought to arise primarily from dust heated by the massive stars in star formation regions and so may be used as a direct estimate of star formation activity. Additional

© 2012 The Authors, MNRAS **424,** 1614–1635
Monthly Notices of the Royal Astronomical Society © 2012 RAS

Downloaded from http://mnras.oxfordjournals.org/ at NASA Goddard Space Flight Ctr on July 14, 2014

contributions are expected to arise from dusty tori surrounding AGN at shorter wavelengths, and there may be non-negligible contributions from the illumination of dust by evolved stars.

Previous surveys from space-based observatories – *IRAS* (e.g. Saunders 1990; Oliver, Rowan-Robinson & Saunders 1992), *ISO* (e.g. Elbaz et al. 1999; Oliver et al. 2002, and references therein) and *Spitzer* (e.g. Shupe et al. 2008; Frayer et al. 2009, and references therein) – and at submm wavelengths from the ground with Submillimetre Common-User Bolometer Array (SCUBA) at 850 μm (e.g. Smail, Ivison & Blain 1997; Hughes et al. 1998; Eales et al. 1999; Coppin et al. 2006), Bolocam (e.g. Maloney et al. 2005a), SHARCII (e.g. Khan et al. 2007), Max Planck Millimeter Bolometer (MAMBO; e.g. Greve et al. 2008), the Large Apex Bolometer Camera (LABOCA; e.g. Weiß et al. 2009) and AzTEC (e.g. Scott et al. 2010b) demonstrated strong evolution in galaxies at both mid-IR (MIR) and FIR wavelengths. This evolution is attributed to a decline in the average star formation density with time, and particularly a decline in the role of the more luminous IR galaxies (LIRGs), which are thought to be the progenitors of massive galaxies today (e.g. Le Floc'h et al. 2005).

This strong evolution has been challenging for physical models of galaxy formation to reproduce. They find they must invoke drastic modifications, such as altering the initial mass function (e.g. Baugh et al. 2005), in order to match these observations as well as optical and near-IR (NIR) constraints on the stellar mass today.

Using a different approach, phenomenological galaxy population models attempt to describe what is currently observed and also predict what we would expect for *Herschel*. Different groups use different combinations of galaxy populations to reproduce the observations; for example, Lagache, Dole & Puget (2003, and Fig. 1) use two peaks of luminosity density at $z \sim 1$ and ~ 2 to describe the data, which are not seen in other models. Such differences between the pre-*Herschel* models indicate the lack of constraint on the SEDs and redshift distributions.

The potential of submm surveys has been demonstrated by the *BLAST* telescope (Devlin et al. 2009). *BLAST* was a balloon-borne telescope with a focal plane instrument based on the SPIRE (Griffin et al. 2010) photometer design and using similar detectors tailored to higher photon loading, and was a successful technical and scientific pathfinder for SPIRE on *Herschel*, probing the wavelength regime where the SED of redshifted galaxies and the IR background peak.

The *Herschel Space Observatory* (Pilbratt et al. 2010) is carrying out surveys of unprecedented size and depth, vastly improving the state of observations in this underexplored waveband. The imaging instruments SPIRE (Griffin et al. 2010) and PACS (Poglitsch et al. 2010), which together fully constrain the peak of the FIR/submm background, allow us to thoroughly investigate the sources in the IR background and characterize their total obscured emission (see e.g. Fig. 2).

The *Herschel* Multi-tiered Extragalactic Survey (HerMES[1]) is a Guaranteed Time Key Programme on *Herschel* which will provide a legacy survey of star-forming galaxies over the wavelengths at which the galaxies and IR background peak. The majority of science goals require multiwavelength support and the fields we have chosen are among the best in the sky for multiwavelength coverage (see Section 4.2) maximizing their legacy value.

In Section 2, we define the survey. In Section 3, we described some of our goals and early results. In Section 4, we outline our expected data products and delivery time-scales before concluding in Section 5.

[1] http://hermes.sussex.ac.uk. Hermes is also the Olympian messenger god, ruler of travellers, boundaries, weights and measures.

2 SURVEY DESIGN

Our survey is defined by Astronomical Observing Requests (AORs). For convenience we have grouped the AORs by sets, which in this paper are identified with numbers, e.g. ELAIS N2 SWIRE is #41. A summary of the AOR sets is given in Table 1. Details of the observing modes can be found in the *Herschel* observers' manuals (available from http://herschel.esac.esa.int/Documentation.shtml).

Detector hit maps,[2] which accurately define the coverage of the survey and should be used for any detailed planning of complementary surveys, are provided on our website http://hermes.sussex.ac.uk. We also provide files which define the approximate boundaries of homogenous regions. These survey definition products are updated as the survey progresses. Our sensitivities have been quoted using official mission values given in Table 3.

The current AORs which define our programme can be retrieved from the *Herschel* Science Archive, http://herschel.esac.esa.int/Science_Archive.shtml, using the *Herschel* Observation Planning Tool (HSPOT) and the proposal IDs SDP_soliver_3 and KPGT_soliver_1 and GT2_mviero_1.

Here we summarize the basis of our survey design.

2.1 Requirements

HerMES was designed to fulfil multiple objectives, which are outlined in Section 3. The *Herschel* bands can probe the peak of the FIR SEDs of star-forming galaxies and thus measure the IR luminosity, $L_{\rm IR}$ (see Fig. 2 and Table 2). Our primary criterion was to sample the ($L_{\rm IR}$, z) plane of star-forming galaxies uniformly and with sufficient statistics to a redshift of $0 < z \lesssim 3$. Specifically, we take a bin resolution of $\Delta \log L_{\rm IR}\, \Delta z = 0.1$ (e.g. $\Delta \log L_{\rm IR} = 0.5$, $\Delta z = 0.2$) and require 75 galaxies per bin to give 12 per cent accuracy (or 10 per cent accuracy when further divided into three subsamples). This resolution corresponds to the scale of features in the luminosity density surface from the Lagache et al. (2003) model, for example. Using the model luminosity functions, we can calculate the area needed to reach this goal for each luminosity and redshift. Each tier thus probes a given ($L_{\rm IR}$, z) region bounded by the areal constraint and the flux limit (see Fig. 1). An optimized sampling over wavelength is achieved by combining HerMES with the PACS Evolutionary Probe (PEP; Lutz et al., 2011) survey.

HerMES was thus designed to comprise a number of tiers of different depths and areas (Tables 5 and 7). HerMES samples the higher luminosity objects, which are bright but rare, in the wide shallow tiers, and the lower luminosity galaxies, which are faint but common and confused, in the deep narrow tiers. Our design has evolved during the mission, but since our initial design had cluster observations (nominally deep, shallow and high-z) and six nominal levels from deep and narrow Level 1 to wide and shallow Level 6, we will maintain those descriptions even though the depths have changed.

[2] These maps and Table 1 give coverage for SPIRE observations as counts of 250 μm detector samples per 6×6 arcsec^2 pixel. This can be converted to a bolometer 'exposure' time per pixel by dividing by the sampling frequencies of 18.6 Hz for SPIRE scanning at nominal and fast rates and 10 Hz for parallel mode. The hits in other arrays can be estimated by scaling by the numbers of detectors in the arrays (129, 88, 43) and the pixel sizes (6, 10, 12 arcsec).

Downloaded from http://mnras.oxfordjournals.org/ at NASA Goddard Space Flight Ctr on July 14, 2014

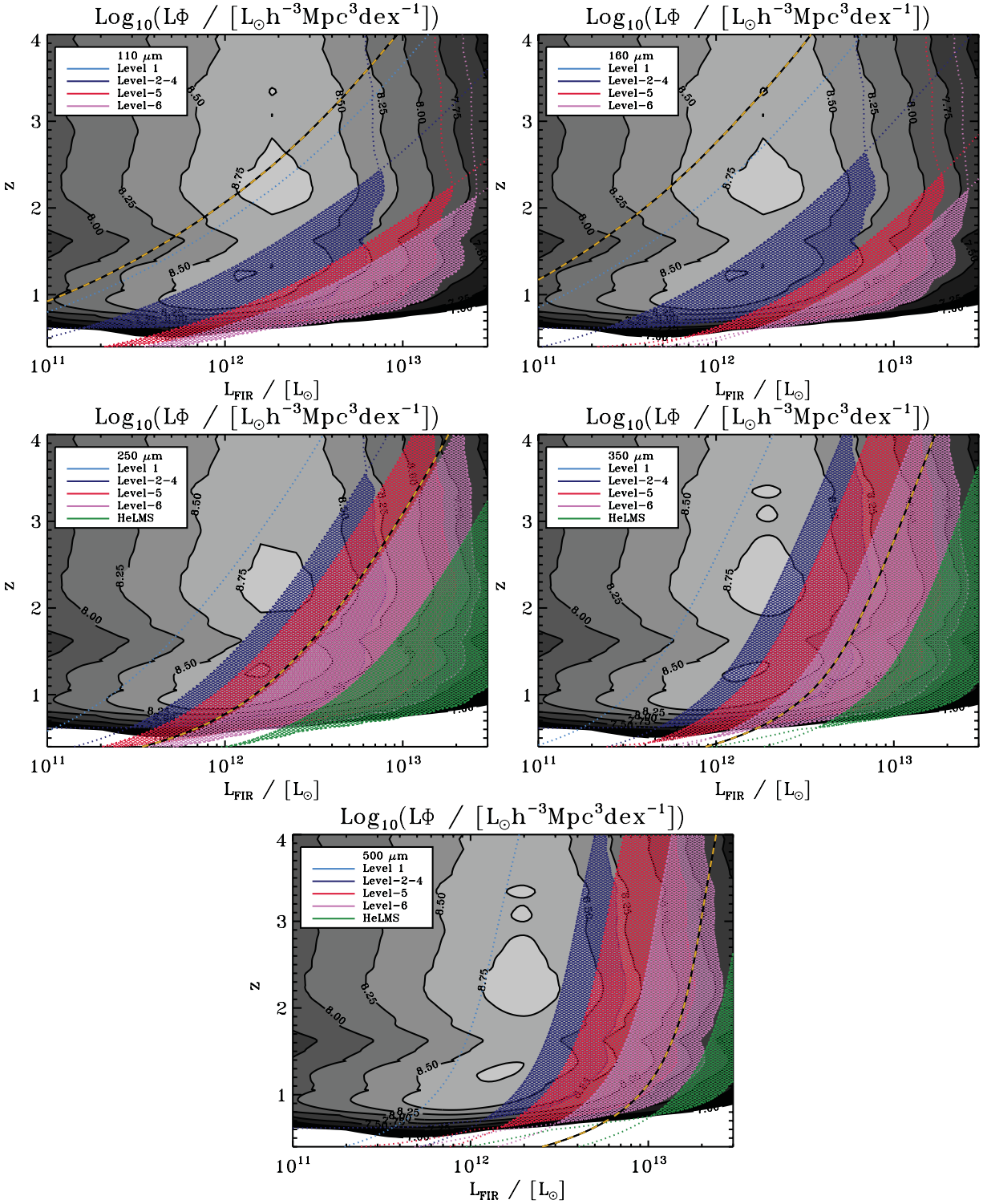

Figure 1. FIR luminosity density in $\log_{10}$ ($L_\odot\, h^{-3}$ Mpc^3 dex^{-1}) (grey-scale and contour diagram) as a function of FIR luminosity (x-axis) and redshift (y-axis) – from the model of Lagache et al. 2003. The powers of different survey elements to probe this space are indicated by overlays. Each panel shows survey elements at different wavelengths; reading left-to-right from the top they are 100, 160, 250, 350 and 500 μm. Surveys are deemed to properly sample the space if they can detect galaxies of these FIR luminosities at the 5σ instrumental noise level and with more than 75 galaxies in bins of $\Delta \log L\, \Delta z = 0.1$. These two constraints are marked with dotted lines and are hatched. The different survey levels defined in Table 7 are shown with blue (Levels 2–4), red (Level 5), magenta (Level 6) and green (HeLMS). Level 1 (cyan) does not have enough volume to satisfy the number of galaxies criterion and so only the instrumental noise limit is shown. The 5σ confusion noise levels (after 5σ clipping) from Berta et al. (2011, at 100 and 160 μm) and Nguyen et al. (2010, at 250, 350 and 500 μm) are shown with yellow/black lines. Note the bimodal peaks at $z \sim 1$ and $\sim$2.5.

Downloaded from http://mnras.oxfordjournals.org/ at NASA Goddard Space Flight Ctr on July 14, 2014

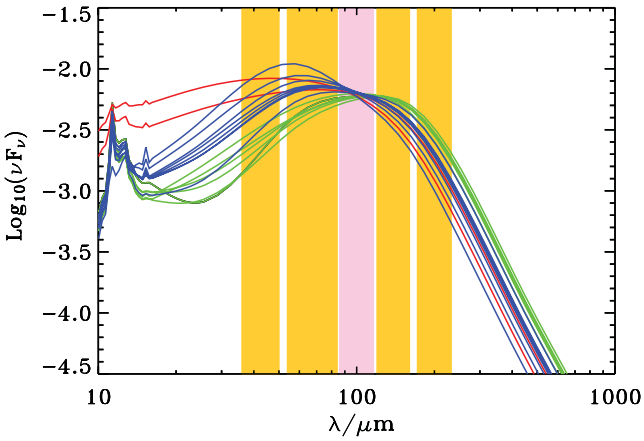

Figure 2. Model spiral (green), starburst galaxy (blue) and AGN (red) SEDs normalized to the same $L_{\rm FIR}$ and plotted in their rest frame with the *Herschel*-PACS and *Herschel*-SPIRE bands at $\lambda = 100, 160, 250, 350$ and 500 μm plotted at $\lambda/(1+z)$ for a galaxy at $z = 1.5$. Note that the *Herschel*-SPIRE band at 250 μm measures a similar flux density for all and so is a reasonable proxy for the $L_{\rm FIR}$ for these templates.

Confusion is a serious issue for *Herschel* and SPIRE in particular, and is an important driver in deciding survey depth (Table 5). To estimate the confusion level, we assembled galaxy models (e.g. Lagache et al. 2003), compared them to existing survey data and calculated the confusion limit using the criteria for source density of 30 beams per source and width of the sky intensity distribution. We employ a number of techniques to overcome the problem of confusion. It is those analyses which motivate the deepest tiers: the lensed clusters fields, and the fast scanned elements of the wide Level 5 tier.

An additional consideration is the volume of the survey needed for a representative sample of the Universe, to provide a sufficient range of environments, and enough independent regions to study clustering (e.g. Fig. 3). Examination of each of those requirements requires survey comoving volumes of 10^6–10^7 Mpc^3 or larger. For example, the number density today of haloes of dark matter mass $M_{\rm DM} > 10^{15}$ M$_\odot$ is around $10^{-6}\,h^3$ Mpc^{-3}(Mo & White 2002). This is identical to the comoving number density of their progenitors, i.e. ∼0.3–0.4 deg^{-2}, for survey shells of $\Delta z = 0.1$. This provides additional motivation for fields of the order of 10 s deg^2 to provide statistical samples. Sampling variance would still be an issue if the smaller deeper levels were contiguous, so we split these into a number of fields to enable us to reduce and estimate the sampling variance errors.

The SPIRE and PACS depths for the cluster observations were determined by the desire to ensure the detection of $z \simeq 3$ sources in both the SPIRE 250 μm and PACS 100 μm channels.

2.2 Choice of fields

In order to pursue multiwavelength analyses, we have selected fields (Fig. 4 and Table 5) which are among the most intensively observed at all wavelengths. These include radio (Very Large Array, Westerbork Synthesis Radio Telescope, Giant Metrewave Radio Telescope, Australia Telescope Compact Array), submm (SCUBA, Bolocam, AzTEC, MAMBO), MIR and FIR (*Spitzer*, *ISO*, *AKARI*), NIR (United Kingdom Infrared Telescope, Visible and Infrared Survey Telescope for Astronomy (VISTA), optical [*Hubble Space Telescope* (*HST*), Subaru Suprime-Cam, Canada–France–Hawaii Telescope MegaCam, Kitt Peak National Observatory Mosaic-1, Cerro Tololo Inter-American Observatory Mosaic-2, Isaac Newton Telescope Wide-Field Camera], UV [Galaxy Evolution Explorer (GALEX)] and X-ray (*XMM–Newton Chandra*). A description of ancillary data is given in Section 4.2. Extensive redshift and/or photometric redshift surveys are either available or underway for most of these fields.

An additional consideration was that the contamination from Galactic emission (or cirrus) should be minimal. The larger mirror means that this cirrus is less of a concern for extragalactic surveys with *Herschel* than it was for *Spitzer*, as discussed in Oliver (2001). This means that our requirement for low levels of cirrus is automatically satisfied by our criteria of good ancillary data, as illustrated in Fig. 4.

The defining criterion was coverage at MIR/FIR wavelengths not accessible to *Herschel*, or where *Herschel* is relatively inefficient due to its warm mirror. Specifically, we required Multiband Imaging Photometer for Spitzer (MIPS) coverage at 24 and 70 μm. At the time of design, the one exception to this was the *Akari Deep Field*-South (ADFS), which did not have *Spitzer* coverage but did have coverage at 65, 90, 140 and 160 μm from *Akari* (Matsuura et al. 2010). However, this field has since been observed by *Spitzer* MIPS (Scott et al. 2010a). The HeRMES Large-Mode Survey (HeLMS) field, which was added in 2011 for studying large-scale structure and the bright end of the number counts, does not have ancillary data from *Spitzer*. However, being located on the Sloan Digital Sky Survey (SDSS) stripe 82 region, HeLMS does have ancillary coverage from many other facilities.

A detailed discussion of the specific observations which were considered in the design of the fields is given in Appendix A.

The deep and shallow cluster targets are well-studied strong lenses at modest redshift. They were selected in consultation with the PEP team – with HerMES carrying out the SPIRE observations and PEP the corresponding PACS observations. The high-z clusters were selected for environmental studies also in consultation with the PEP team.

2.3 Observing modes

The mapping of Levels 1–4 (#1,11–19, 22, 23) is performed using SPIRE 'Large Map' mode. This mode is described in detail in the SPIRE Observers' Manual.[3] This is the default SPIRE observing mode for any field size larger than 4×4 arcmin^2. In this mode, maps are made by scanning the telescope because it eliminates off-beam confusion, allows measurement of extended emission and increases observing efficiency for larger fields. Since our smallest blank field to be mapped (Level 1) is $\sim 16 \times 16$ arcmin^2, this mode was the natural choice for our programme.

The SPIRE cluster observations were originally designed using the 'Large Map' mode covering a nominal field of 4×4 arcmin^2 as this was the smallest map that could be made using scanning. Abell 2218, #1, was carried out in that mode. We moved to 'Small Map' mode (#2–10) in which the map is made by two short cross-scans with the telescope once that became available, as that was more efficient for small fields.

When building maps, the telescope is scanned at an angle of 42°.4 with respect to the z-axis of the arrays (see figs 3.1 and 3.3 of the SPIRE Observers' manual, V2.4). This produces a fully sampled map, despite the focal plane not being fully sampled. The offset between successive scans (or scan 'legs') is 348 arcsec, nearly

[3] The SPIRE Observers Manual is available from the Herschel Science Centre http://herschel.esac.esa.int/Docs/SPIRE/html/spire_om.html

Downloaded from http://mnras.oxfordjournals.org/ at NASA Goddard Space Flight Ctr on July 14, 2014

Table 1. Summary of the HerMES observations. The full set of AORs is available through ESA's *Herschel* archive. We have grouped $N_{\rm AOR}$ observations of the same field at the same level made with the same mode and areal size into a 'set' (the number of AORs still to be scheduled after 2011 December 21 is indicated in parentheses). The first five columns in the table give the set identification number, the design level, the target name, the *Herschel* observing mode and the number of AORs in the set. T is the time used or allocated for this set. $N_{\rm rep}$ is the total number of repeats of the observing mode in the set. All our SPIRE nominal (30 arcsec s^{-1}) and fast mode (60 arcsec s^{-1}) (Sp. Nom. and Sp. Fast) observations include a scan in the nominal and orthogonal direction, so one repeat is two scans. For SPIRE observations that have been executed, $N_{\rm samp}$ is the median number of bolometer samples per pixel in the 250 μm map (6×6 arcsec^2 pixels). This can be converted to exposure time per pixel or to other bands as described in footnote 2. The error per pixel in our SPIRE maps as processed by the standard HIPE pipeline are $\sigma_{250}^2 = \sigma_0^2/N_{\rm samp}$, with $\sigma_0^2 = 896 \pm 11$, 1554 ± 27 and $\sim$1440 mJy^2 beam^{-2} for parallel, Sp. Nom. and Sp. Fast modes, respectively. l_1, l_2 are sides of a rectangle with near homogenous coverage. θ is the roll angle with short axis of that rectangle measured east of north. For SPIRE observations that have been executed, $\Omega_{\rm max}$ is the total area of pixels with any 250 μm coverage and $\Omega_{\rm good}$ is the area of pixels where the number of bolometer samples per pixel in the 250 μm map is greater than $N_{\rm samp}/2$. For PACS fields or unobserved SPIRE fields, $\Omega_{\rm nom}$ gives the nominal area of region. The final column indicates which observations are included in our data releases; observations marked SDP were released in our Early Data Release, observations marked SDP or DR1 were released in our First Data Release. Set numbers #16 and #26 were removed from the programme.

Set	Level	Target	Mode	$N_{\rm AOR}$	T (h)	$N_{\rm rep}$	$N_{\rm samp}$	l_1 (arcmin)	l_2 (arcmin)	θ (°)	$\Omega_{\rm nom}$ (deg^2)	$\Omega_{\rm max}$ (deg^2)	$\Omega_{\rm good}$ (deg^2)	DR
1	CD	Abell 2218	Sp. Nom.	2	9.29	100	1118	4	4	84		0.14	0.10	SDP
2	CD	Abell 1689	Sp. Nom.	8	1.97	48	235	4	4	18		0.11	0.08	
3	CD	MS 0451.6−0305	Sp. Nom.	8	1.97	48	235	4	4	5		0.11	0.08	DR1
4	CS	RX J13475−1145	Sp. Nom.	8	1.97	48	234	4	4	17		0.11	0.08	
5	CS	Abell 1835	Sp. Nom.	8	1.97	48	236	4	4	16		0.11	0.08	
6	CS	Abell 2390	Sp. Nom.	8	1.97	48	235	4	4	81		0.11	0.08	
7	CS	Abell 2219	Sp. Nom.	8	1.97	48	234	4	4	66		0.11	0.08	DR1
8	CS	Abell 370	Sp. Nom.	8	1.97	48	233	4	4	70		0.11	0.08	
9	CS	MS 1358+62	Sp. Nom.	8	1.97	48	235	4	4	76		0.11	0.08	
10	CS	Cl0024+16	Sp. Nom.	8	1.97	48	235	4	4	61		0.11	0.08	
11	CH	MS 1054.4−0321	Sp. Nom.	8	2.18	16	131	15	10	22		0.24	0.16	
12	CH	RX J0152.7−1357	Sp. Nom.	8	2.18	16	131	15	10	165		0.24	0.16	
13	L1	GOODS-S	Sp. Nom.	76	20.22	76	730	20	20	14		0.51	0.35	
22	L2	COSMOS	Sp. Nom.	24	50.13	24	388	85	85	70		3.49	2.82	
14	L2	GOODS-N	Sp. Nom.	1	13.51	30	416	30	30	42		0.64	0.55	SDP
15	L2	ECDFS	Sp. Nom.	19	8.78	19	232	30	30	44		0.79	0.58	DR1
17	L3	Groth Strip	Sp. Nom.	7	3.54	7	85	67	10	130		0.82	0.60	DR1
18	L3	Lockman-East *ROSAT*	Sp. Nom.	7	3.2	7	87	30	30	77		0.77	0.57	
18B	L3	Lockman-East *Spitzer*	Sp. Nom.	4	4.53	4	32	80	40	149		1.78	1.40	
19	L3	Lockman-North	Sp. Nom.	1	3.91	7	104	35	35	1		0.74	0.65	SDP
23	L4	UDS	Sp. Nom.	7	10.54	7	110	66	66	20		2.46	2.02	
24	L4	VVDS	Sp. Nom.	7	10.39	7	110	66	66	21		2.46	2.02	
22B	L5	COSMOS HerMES	Sp. Nom.	8	25.20	8	128	110	110	70		5.04	4.38	
27	L5	CDFS SWIRE	Sp. Fast	10	41.72	20	81	190	150	99		12.18	11.39	
28	L5	Lockman SWIRE	Sp. Fast	2	13.51	2	16	218	218	2		18.2	17.37	SDP
28B	L5	Lockman SWIRE	Sp. Fast	8	41.26	8	58	220	180	50		15.26	7.63	
42	L7	HeLMS	Sp. Fast	11(10)	103.4	2		1560	750	15	270			
20	L3	Lockman-North	PACS	12	13.96	11		30	30	42	0.25			SDP
20B	L3	Lockman-North	PACS	20	20.89	20		30	30	42	0.25			
21	L3	UDS HerMES	PACS	25	25.93	14		30	30	0	0.25			
25	L4	UDS	PACS	12	40.19	7		57	57	0	0.9			
29	L5	EGS HerMES	Parallel	7	22.68	7	93	150	40	131		3.50	2.67	
30	L5	Bootes HerMES	Parallel	5	20.33	5	70	80	80	0		4.21	3.25	DR1
31	L5	ELAIS N1 HerMES	Parallel	5	20.82	5	72	95	95	38		3.74	3.25	DR1
32	L5	*XMM* VIDEO1	Parallel	4	13.44	4	65	106	75	107		3.20	2.72	
32B	L5	*XMM* VIDEO2	Parallel	4	8.88	4	53	106	44	107		2.12	1.74	
32C	L5	*XMM* VIDEO3	Parallel	4	13.44	4	53	106	75	107		3.19	2.73	
33	L5	CDFS SWIRE	Parallel	4	50.42	4	57	204	170	101		11.87	10.89	
34	L5	Lockman SWIRE	Parallel	4(2)	71.22	4		215	215	154		17.86	16.08	
39B	L5	ELAIS S1 VIDEO	Parallel	4	17.72	4	56	138	80	87		4.42	3.72	
35	L6	ELAIS N1 SWIRE	Parallel	2	28.0	2	28	207	192	55		13.37	12.28	
36	L6	*XMM*-LSS SWIRE	Parallel	6	45.58	2	29	180	180	82		21.62	18.87	DR1
37	L6	Bootes NDWFS	Parallel	4	27.99	2	30	243	80	145		11.3	10.57	DR1
38	L6	ADFS	Parallel	2	18.11	2	28	190	122	80		8.58	7.47	DR1
39	L6	ELAIS S1 SWIRE	Parallel	2	17.9	2	28	140	81	91		8.63	7.86	
40	L6	FLS	Parallel	2	17.1	2	29	160	138	5		7.31	6.71	SDP
41	L6	ELAIS N2 SWIRE	Parallel	2	17.1	2	26	177	119	147		9.06	7.80	

Downloaded from http://mnras.oxfordjournals.org/ at NASA Goddard Space Flight Ctr on July 14, 2014

Table 2. Basic band information for the different *Herschel* channels used by HerMES. Data are taken from SPIRE and PACS Observers' Manuals V2.4/V2.3 (respectively).

	At nominal wavelength (μm)				
	100	160	250	350	500
Instrument	PACS	PACS	SPIRE	SPIRE	SPIRE
Filter name	Blue2	Red	PSW	PMW	PLW
Min λ (μm)	85	125	210	300	410
Max λ (μm)	125	210	290	400	610

Table 3. Point source sensitivities for different *Herschel* observing modes. Scan rates are given for each mode; we also tabulate the step size between successive scan legs (predetermined for SPIRE and parallel mode but user-defined for PACS). In parallel mode, the step size are different for maps built by scanning in each of the two 'orthogonal' directions. 5σ sensitivities in units of (mJy $\sqrt{N_{\rm scan}}$) for a single scan are estimated from the HSPOT v5.1.1. Modes below the line are not used by HerMES but by other Key Programme surveys.

Mode	Rate (arcsec s^{-1})	Step (arcsec)	5σ sensitivities (mJy $\sqrt{N_{\rm scan}}$) at wavelength (μm)				
			100	160	250	350	500
SPIRE	30	348			64	53	76
SPIRE	60	348			91	75	108
PACS	20	55	42	80			
Parallel	20	168/155	71	135	37	30	44
Parallel	60	168/155	122	232	63	53	75

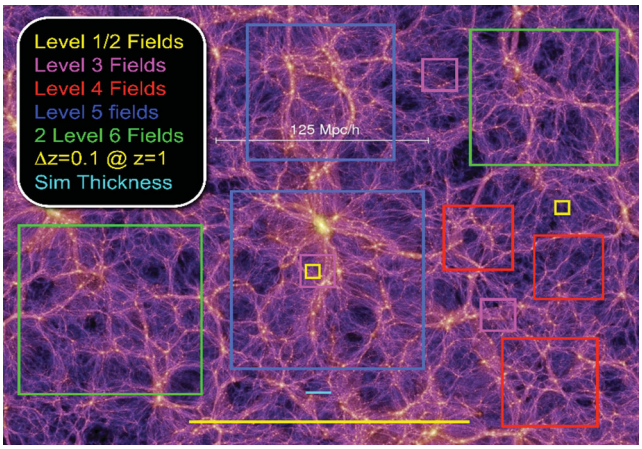

Figure 3. A slice of the dark matter in the Millennium Simulation of the Universe, seen today (Springel et al. 2006). Overlayed are the footprints of some of our fields, showing how much of this slice they would sample at $z = 1$. This thin slice exaggerates the effect but illustrates that to overcome sampling variance and to probe a full range of environments we need multiple, large fields.

the full projected array size (see fig. 3.2 of the SPIRE Observers' manual, V2.4). SPIRE observations use two near-orthogonal default scan angles i.e. $\pm 42\overset{\circ}{.}4$.

Multiple map repeats were required to integrate down to the flux limit in each level. These repeats were performed with as much cross-linking as possible (i.e. with similar numbers of scans in quasi-orthogonal directions), to enable mapping with the presence of low-frequency drifts and redundancy for the removal of any problematic scans. We used the nominal SPIRE scan rate of 30 arcsec s^{-1} for these fields.

Where long observations had to be split, we aimed to cover the whole field on separate occasions (rather than dividing the field and subsequently building a mosaic) to give redundancy and maximal cross-linking.

The Lockman SWIRE and CDFS SWIRE observations in Level 5 (#27 and 28) were motivated by the study of extragalactic background fluctuations.

These observations required the rapid scanning using the SPIRE fast scan rate at 60 arcsec s^{-1} to minimize the effects of low-frequency drifts and increase redundancy. The scanning angles and scan leg offsets are the same as for the nominal scan rate.

The knee frequency is that at which the power of the correlated fluctuations (primarily from the thermal drifts) equates to the white noise. The design goal for the SPIRE detectors was for the knee to be at 30 mHz (with a requirement of 100 mHz) but the in-flight performance is much better, and by using the thermometer signals to de-correlate, the drifts knee frequencies of 1–3 mHz can be recovered (Griffin et al. 2010). The drift is correlated across the detector array (139 bolometers at short wavelengths) and so the effective knee frequency for maps is higher. Assuming the knee frequency to be 30 mHz, thermal drift effects would impact on a spatial scale of 33 arcmin (for the fast scan rate) compared to 17 arcmin for the nominal scan rate.

Levels 5 and 6 (#29–41 and 22B) are being mapped with the SPIRE-PACS parallel mode. This mode is described in detail in the SPIRE-PACS Parallel Mode Observers' Manual.[4] Parallel mode maps the sky simultaneously with both instruments. The SPIRE detector sampling rate is reduced from 18.2 to 10 Hz in this mode, which has a negligible impact when scanning in the slow (20 arcsec s^{-1}) mode. For the blue channel of the PACS instrument we used the PACS Blue2 85–125 μm filter (rather than the 60–85) for maximum sensitivity. We used the 20 arcsec s^{-1} scanning mode as the 60 arcsec s^{-1} mode was not suitable for PACS as the beam is degraded by up to 30 per cent (Poglitsch et al. 2010, and Table 4).

The parallel mode achieves the combined PACS and SPIRE sensitivities more efficiently for large areas than observations using each instrument in turn. Scan directions alternate between nominal and orthogonal for maximal cross-linking.

The Level 7, HeLMS, observations (#42) exploited the ability of the SPIRE to make long (20°) scans at the fast (60 arcsec s^{-1}) scan rate. These were interleaved in a cross-like configuration to give duplicate coverage in a near-orthogonal direction. The resulting 270 deg^2 maps are thus optimized for studying fluctuations on the largest possible scale.

All PACS-only observations (Levels 3–4, #20, 21, 25, 26) were carried out using the scan mapping mode. This mode is described in detail in the PACS Observers' Manual.[5]

The noise of the PACS bolometer/read-out system has a strong $1/f$ component (Poglitsch et al. 2010) and observations need to be modulated on a time-scale of 1–5 Hz. We used the 20 arcsec s^{-1} scan rate in which the beam has full width at half-maximum (FWHM) ∼6.8 or ∼11.3 arcsec in the two bands we use (see Table 4), i.e. sources are modulated on ∼2–3 Hz time-scale. Faster scan rates (e.g. 60 arcsecs^{-1} in parallel mode) would have introduced significant

[4] The SPIRE-PACS Parallel Mode Observers' Manual is available from the Herschel Science Centre http://herschel.esac.esa.int/Docs/PMODE/html/parallel_om.html

[5] The PACS Observers Manual is available from the Herschel Science Centre http://herschel.esac.esa.int/Docs/PACS/html/pacs om.html

Downloaded from http://mnras.oxfordjournals.org/ at NASA Goddard Space Flight Ctr on July 14, 2014

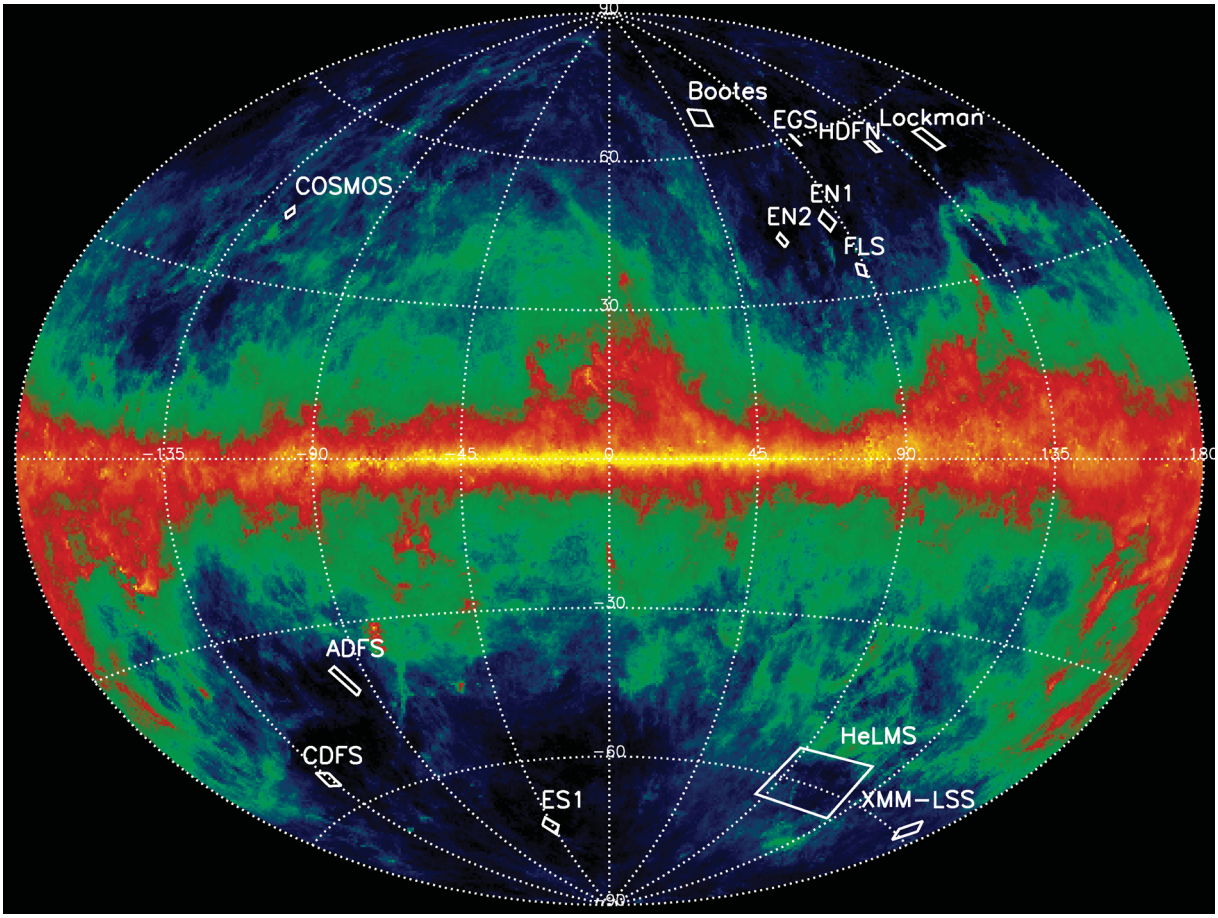

Figure 4. Map of dust emission from the Galaxy, with HerMES fields overplotted. The image is the 100 μm, *COBE*-normalized, *IRAS* map of extended emission (Schlegel, Finkbeiner & Davis 1998). The projection is Hammer–Aitoff in Galactic coordinates. The sky brightness is plotted on a false-colour logarithmic scale, with regions of very low Galactic emission appearing black and the Galactic plane yellow. In addition to the blank fields marked, HerMES has also observed 12 known clusters.

Table 4. Beam sizes for different *Herschel* observing modes. Scan rates are given for each mode. The FWHM of the beams in units of arcsec are taken from SPIRE and PACS Observers' Manuals V2.4/V2.3 (respectively). Where two values are given, these are the major and minor axes; when the ellipticity is less than 15 per cent, the geometric mean of the two is quoted. The SPIRE beam is not known to vary significantly with scan rate and only one value is given. Modes below the line are not used by HerMES but by other Key Programme surveys.

Mode	Rate (arcsec s^{-1})	Beam FWHM (arcsec) at wavelength (μm) 100	160	250	350	500
SPIRE	30/60			18.2	24.9	36.3
PACS	20	6.8	11.4			
Parallel	20	6.8	11.4	18.2	24.9	36.3
Parallel	60	7.0 × 12.7	11.6 × 15.7	18.2	24.9	36.3

beam smearing of around 30 per cent (Poglitsch et al. 2010, and Table 4).

We alternated orthogonal scan directions to minimize correlated noise, i.e. correlations arising from asymmetric transient detector responses to sky signal.

2.4 Dithering

Moving the array on successive scans so that different pixels or bolometers trace different parts of the sky (dithering) improves the quality of the data in a number of ways. Dither steps of more than one detector will reduce correlated noise arising when the same detector crosses the same patch of sky on a short time-scale. Dithering on large scales will also increase uniformity by distributing dead/noisy pixels across the maps. Dithering at subdetector scales can possibly lead to some improvement in resolution if the point spread function is not fully sampled (in the case of SPIRE), further reducing the impact of the sparse filling of the focal plane.

For PACS-only observations, we implemented a dithering pattern. For each scan, we requested an offset with respect to our nominal target position with offsets defined on a grid with spacing (0, ±7.5, ±10.5 arcsec). This provides sampling at subpixel and subarray scales.

For SPIRE, we modelled the scan pattern of good detectors and investigated dithering patterns that reduced the variation in sensitivity to point sources (for details see Appendix B). We found that for a given number of repeats, N, offsetting by a fraction $1/N$ of the scan leg separation between repeats was usually close to optimal. Exceptions to this would be cases where the resulting step size coincided with the projected bolometer spacing; however, none of our patterns resulted in that coincidence. This also provided a

Downloaded from http://mnras.oxfordjournals.org/ at NASA Goddard Space Flight Ctr on July 14, 2014

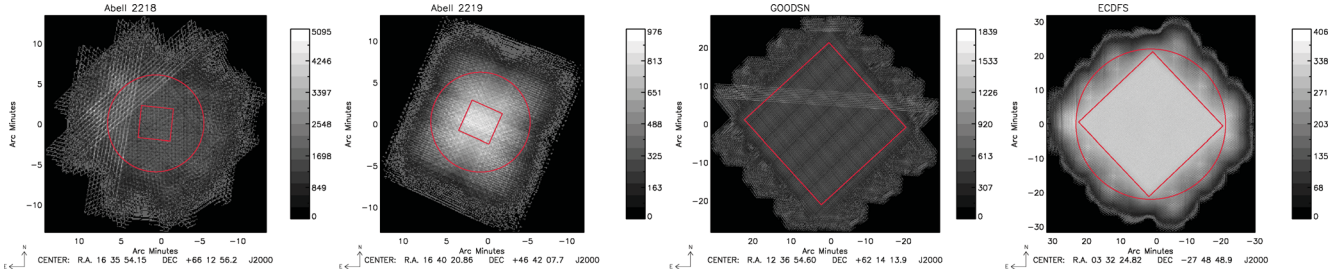

Figure 5. Maps of the number of bolometer samples per pixel of four deep SPIRE 250 μm observations. From left to right: Abell 2218 which was observed in SDP without dithering; Abell 2219 which was taken with dithering; GOODS-N (taken in SDP without dithering) and ECDFS with dithering. FITS files of all coverage maps are on http://hermes.sussex.ac.uk/ as will be new coverage maps as the data are taken.

good de-correlation of the noise. The disadvantage of these large dither steps is that the coverage declines at the edges of the map. However, for our large maps this is not a major penalty. Since each SPIRE-only observation consisted of two scans, one at each of the near-orthogonal SPIRE scan angles, we set an offset in both directions at once. We arranged these offset pairs in a square pattern to minimize the edge effects. This dithering was not done for observations taken during the Science Demonstration Phase (SDP), but was implemented afterwards. The contrast in the coverage maps between dithering and not dithering can be seen in Fig. 5.

2.5 Sensitivity

To estimate the sensitivity of our survey design, we use the HSPOT v5.1.1. For our survey scanning patterns, we compute the 5σ instrument sensitivity (ignoring confusion noise). The HSPOT sensitivities are tabulated in Table 3 and their implications for *Herschel* surveys in Table 5.

2.6 Economies from nesting

We have designed our survey starting at the widest, shallower tier and building up the deeper tiers. Thus, a small field tier nested within a shallower tier needs fewer repeats to reach the required depth. This improves the overall survey efficiency, because observations of small fields are relatively inefficient due to the overheads associated with telescope turnarounds.

The current coverage of the nested fields around CDFS is illustrated in Fig. 6.

The nesting of fields is indicated in columns 5 and 6 in Table 5. and the sensitivities in Table 5 take this into account. For example, UDS-HerMES at Level 3 (#21) includes 12 PACS scans from UDS Level 4 (#25), in addition to the 25 from Level 3, giving a total of 37 as well as 14 SPIRE nominal scans from UDS Level 4 (#23), four Parallel scans from *XMM*-VIDEO at Level 5 (#32) and two parallel scans from Level 6 *XMM*-LSS SWIRE (#36).

2.7 Total time

The total time allocated for HerMES is 909.3 h. This comes from the Guaranteed Time awarded to the SPIRE instrument team (850 h), one of the *Herschel* mission scientists (M. Harwit, 10 h) and members of the *Herschel* Science Centre (B. Altieri, L. Conversi, M. Sanchez Portal and I. Valtchanov, 40 h). ESA also effectively contributed 9.3 h as we agreed for our Abell 2218 observations in SDP to be made public immediately and so were not charged for these observations.

2.8 Special requirements and constraints

The *Herschel* observatory is performing very close to specifications and our survey design is very similar to the one proposed. However, some changes and compromises have been made on the basis of post-launch experience.

Early in the mission, there was a constraint that parallel mode observations could not exceed 2^{15} s, as this exceeded the limit of one software counter. Since each parallel mode observations was already a single scan, they were as shallow as could be done at that scan rate, so this required us to split some of the Level 5 and 6 fields into smaller fields, compromising the uniformity of the data. The impact of this on the coverage for the *XMM*-LSS and Boötes fields is shown in Fig. 7. The planned ADFS (#41) and ELAIS S1 (#39) fields required only slightly more time than 2^{15} s, and so we chose to reduce the field size rather than split the field.

Where the orientation of the SPIRE data with respect to complementary data was particularly important, we constrained the observations to align with them. Solar avoidance constraints meant that it was not possible to align the SPIRE observations of *XMM*-LSS SWIRE (#36) and COSMOS (#22) optimally with the *Spitzer* data and PEP data, respectively. For *XMM*-LSS SWIRE, we observed a larger field containing the *Spitzer* data, while for COSMOS we observed a larger shallower field, COSMOS HerMES (#22B), containing the planned PEP PACS observations and a smaller deeper field (COSMOS, #22), which does not fully cover the PACS observations.

The *Spitzer*-Extragalactic Representative Volume Survey (SERVS; Lacy et al. 2009) and the Visible and Infrared Survey Telescope for Astronomy (VISTA) – Deep Extragalatic Observations Survey (VIDEO; Bomfield et al. 2010) were approved after HerMES and designed with reference to HerMES. So, almost all the SERVS and VIDEO fields were included in our Level 5 observations. However, the SERVS and VIDEO field in ELAIS S1 was not quite within our planned observations, which were only at Level 6. We thus included additional deeper observations covering the SERVS/VIDEO field (#39B).

Our initial SDP observations of Abell 2218 used 'Large Map' mode as this was the only way of doing scan mapping. We changed our deep cluster observations to the 'Small Map' mode once the mode was available.

The $P(D)$ results of Glenn et al. (2010) successfully probed the number counts well below the confusion limit, reducing the motivation for exceptionally deep cluster observations. We have thus reduced the number of repeats.

Due to an error in entering the AOR, one parallel observation scan of ELAIS S1 SWIRE (#39) was accidentally observed with the shorter wavelength 60–85 μm channel rather than the 85–125 μm channel.

Downloaded from http://mnras.oxfordjournals.org/ at NASA Goddard Space Flight Ctr on July 14, 2014

Table 5. HerMES survey with sensitivities in the context of other survey programmes being undertaken by *Herschel*. The 'observations' columns refer to the AOR set numbers of Table 1 for HerMES or for other Key Programmes we use: 'E' for Egami cluster programme, 'G' for H-GOODS, 'P' for PEP, 'A' for H-ATLAS and 'S' for the Carlstrom et al. programme (see Table 6). The sensitivities are estimated consistently using HSPOT v5.1.1. These are single pixel sensitivities and ignore the benefits of matched filters, particularly for unconfused fields, e.g. H-ATLAS quote empirical 5σ sensitivities of 105, 140, 32, 36, 45 mJy for the five wavelengths, so the sensitivities in this table should be scaled by 1.22, 0.85, 0.72, 0.97, 0.85 to obtain a consistent comparison with H-ATLAS. The sensitivity of HerMES observations has been calculated including data from shallower tiers as described in the text. Other surveys are treated independently. Cluster observations are listed before blank fields. The fields are ordered in increasing 250 μm flux limit, then right ascension. The area is defined by the PACS observations for Levels 1–4 (above the second horizontal line), otherwise we use Ω_{good} from Table 1 or Ω_{nom} for HeLMS. We tabulate three areas: the nominal area for each field; the 'doughnut' area which excludes any deeper subfields within and the cumulative area of all fields higher in the table. The 5σ confusion noise (after 5σ cut) from Nguyen et al. (2010) is 24.0, 27.5, 30.5 mJy (at 250, 350 and 500 μm), approximately the Level 6 depth. GOODS-S also has PACS data not listed here at 70 μm over 0.11 deg^2 to a 5σ depth of 1.9 mJy.

Fields	Area Nominal	Extra (deg^2)	Cumulative	Observations PACS	SPIRE	5σ noise level (for band in μm) 110	160	250 (mJy)	350	500
Abell 2218	0.0050	0.0050	0.1	P	1	4.1	7.9	6.4	5.3	7.6
Abell 1689	0.0050	0.0050	0.11	P	2	3.6	6.9	9.2	7.7	11.0
Eight targets	0.04	0.04	0.15	P	3–10	5.7	10.9	9.2	7.7	11.0
Two targets	0.03	0.03	0.18	P	11–12			13.9	11.6	16.7
Various	0.18	0.18	0.36	E	E	6.1	11.7	14.2	11.9	17.1
GOODS-N	0.042	0.042	0.04	G,P	G,14	2.2	4.1	3.8	3.1	4.5
GOODS-S	0.11	0.087	0.13	G,P,33	13,15,27,33	2.1	2.9	4.3	3.6	5.2
GOODS-S	0.012	0.012	0.14	G,P,33	13,15,27,33	1.1	2.1	4.6	3.8	5.5
GOODS-S	0.018	0.0060	0.15	G,P,33	13,15,27,33	1.6	3.0	4.6	3.8	5.5
GOODS-S	0.023	0.0060	0.15	G,P,33	13,15,27,33	2.0	3.8	4.6	3.8	5.5
COSMOS	2.0	2.0	2.15	P	22,22B	7.7	14.7	8.0	6.6	9.5
ECDFS	0.25	0.14	2.29	P,33	15,27,33	7.6	14.5	8.0	6.6	9.6
GOODS-N	0.25	0.208	2.5	P	14	4.7	8.9	8.2	6.8	9.9
Lockman-East	0.25	0.25	2.75	P	18,18B,28B,34,28	6.5	12.3	9.6	7.9	11.5
Lockman-North	0.25	0.25	3.0	20,20B,34	19,28B,34,28	7.4	14.1	10.6	8.8	12.7
Groth Strip	0.25	0.25	3.25	P,29	17,29	7.1	13.6	10.7	8.9	12.8
UDS HerMES	0.25	0.25	3.5	21,25,32,36	23,25,32,36	6.8	12.9	11.2	9.3	13.4
UDS	0.7	0.7	4.2	25,32,36	25,32,36	11.2	21.4	11.2	9.3	13.4
VVDS	2.0	2.0	6.2	25,32C,36	25,32C,36	28.8	54.9	11.2	9.3	13.4
CDFS SWIRE	11.4	11.1	17.3	33	27,33	31.5	60.2	12.7	10.5	15.2
Lockman SWIRE	16.1	15.6	32.9	34	28,28B	35.3	67.3	13.6	11.2	16.2
EGS HerMES	2.7	2.5	35.4	29	29	26.6	50.8	13.8	11.3	16.4
Boötes HerMES	3.3	3.3	38.6	30,37	30,37	26.6	50.8	13.8	11.3	16.4
ELAIS N1 HerMES	3.3	3.3	41.9	31,35	31,35	26.6	50.8	13.8	11.3	16.4
ELAIS S1 VIDEO	3.7	3.7	45.6	39B,39	39B,39	28.8	54.9	14.9	12.2	17.8
XMM-LSS VIDEO	7.7	5.0	50.6	32,32B,32C,36	32,32B,32C,36	28.8	54.9	14.9	12.2	17.8
COSMOS Hermes	4.4	2.4	53.0		22B			15.9	13.3	19.1
ELAIS N2 SWIRE	7.9	7.9	60.9	41	41	49.9	95.1	25.8	21.2	30.8
FLS	6.7	6.7	67.6	40	40	49.9	95.1	25.8	21.2	30.8
ADFS	7.5	7.5	75.1	38	38	49.9	95.1	25.8	21.2	30.8
ELAIS S1 SWIRE	7.9	4.2	79.2	39	39	49.9	95.1	25.8	21.2	30.8
ELAIS N1 SWIRE	12.3	9.1	88.3	35	35	49.9	95.1	25.8	21.2	30.8
Boötes NDWFS	10.6	7.3	95.6	37	37	49.9	95.1	25.8	21.2	30.8
XMM-LSS SWIRE	18.9	15.0	110.6	36	36	49.9	95.1	25.8	21.2	30.8
Various	570.0	570.0	681.0	A	A	86.3	164.0	44.5	37.1	53.0
SPT	100.0	100.0	781.0		S			45.3	37.5	54.1
HeLMS	270.0	270.0	1051.0		42			64.0	53.0	76.5

The PACS sensitivity of 10 mJy (5σ in 1 h) in the 85–125 μm channel was significantly less than the pre-launch estimate (5.3 mJy, PACS Observers' manual v1.1) and we removed our planned PACS observations of the VVDS field (#26).

To extend the fluctuation science goals and increase the *Herschel* discovery space for rare objects including gravitationally lensed systems, we added the HeLMS, a wide, SPIRE-only, tier of 270 deg^2 taking around 100 h. This exploits the ability of SPIRE to cover wide areas close to the confusion limit. This additional level is indicated in Table 5.

2.9 Observations

Our first observation was carried out on 2009 September 12. This was the first half of our SPIRE observations of Abell 2218 (#1) and the resulting map from all the data is shown in Fig. 8. This was part of the *Herschel* SDP. Our SDP observations were designed to exercise most of the modes that were to be used in the full survey, and the SPIRE observations are described in Oliver et al. (2010b). This includes the observations of The Great Observatories Origins Deep Survey-North (GOODS-N) (#14; Fig. 9). The SDP

Downloaded from http://mnras.oxfordjournals.org/ at NASA Goddard Space Flight Ctr on July 14, 2014

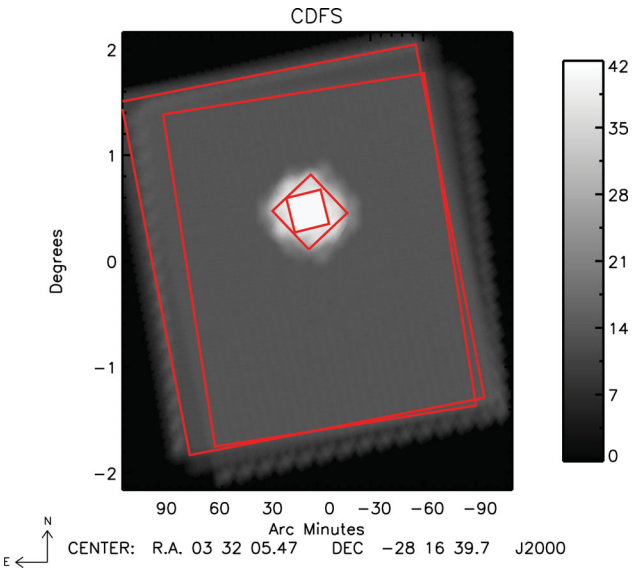

Figure 6. Map of square root of number of effective number of bolometers samples per pixel for SPIRE 250 μm blank-field observations of the CDFS region, which includes our GOODS-S, ECDFS and CDFS-SWIRE observations (#13, 15, 27, 33). The parallel mode samples (#33) have been scaled by the relative sampling rates, 18.6/10, to give the effective number of samples they would have had if the observation had been carried out with SPIRE large-map mode with the same exposure time per pixel. A region of uniform coverage for each of the independent sets is marked with a rectangle. N.B. the total coverage drops off in the north-eastern corner of the largest rectangle (delimiting #33) due to the coverage coming from the boundaries of the large-map mode observations (#27) but is uniform in a coverage map built from #33 data alone.

observations concluded on 2009 October 25; AORs are available under the proposal ID SDP_soliver_3.

The programme is now being carried out as part of the Routine Phase (proposal ID KPGT_soliver_1) and is expected to be completed during 2011. The current ESA schedule is on herschel.esac.esa.int/observing/ScheduleReport.html and the observing log can be followed on herschel.esac.esa.int/observing/LogReport.html.

2.10 Comparison with other *Herschel* surveys

HerMES was planned alongside the PEP survey (Proposal ID KPGT_dlutz_1; e.g. Lutz et al., in preparation). Since then, there have been a number of related Key Project surveys carried out in Open Time. There have also been a few surveys being undertaken in Open Time but not as Key Projects. These programmes are listed in Table 6.

The cumulative area of all major *Herschel*-SPIRE extragalactic Key Programme surveys as a function of instrumental noise (taken from Table 5) and for the HerMES fields is shown in Fig. 10.

It is striking to compare the *Herschel*-SPIRE submm surveys with previous submm surveys. To do this, we have explored the sensitivity of surveys to a canonical galaxy with a modified blackbody SED with emissivity $\beta = 1.5$ and temperature $T = 35$ K. These are shown in Fig. 11.

3 EARLY AND ANTICIPATED SCIENCE

3.1 Confusion limits

An important consideration in design of HerMES was the impact of source confusion at SPIRE wavelengths, i.e. the limited ability to separate individual sources due to the resolution of the telescope and the number density of sources. We define confusion noise to be the standard deviation of the intrinsic variations in a map on the scale of the beam due to all point sources. We planned our survey with reference to several number count models (Lagache et al. 2003; Xu et al. 2003; Le Borgne et al. 2009; Pearson & Khan 2009; Franceschini et al. 2010). We used these models to estimate the fluctuations in a map which at the 4σ level were 1.6 ± 0.9, 10.6 ± 3.1, 26.3 ± 6.3, 32.5 ± 7.5 and 30.0 ± 7.5 mJy at 100, 160, 250, 350 and 500 μm, respectively. The uncertainties come from the scatter between models. The SPIRE confusion noise estimates compare very favourably with the fluctuations in our maps as calculated by Nguyen et al. (2010) with $5\sigma = 24.0$, 27.5, 30.5 mJy at 250, 350 and 500 μm, respectively, after cutting maps at 5σ. This is perhaps fortuitous given that the model counts do not fit the observed counts very well in detail (e.g. Glenn et al. 2010; Oliver et al. 2010b) but may be because the models had been constrained to fit the IR background.

We planned for the survey to have a substantial area (providing SDSS-like volumes) at the confusion limit, but with some regions well below the confusion limit in very well studied fields, to exploit techniques for mitigating confusion using high signal-to-noise ratio (S/N) data.

3.2 Science above the confusion limit

3.2.1 Direct determination of the total far-infrared luminosity function and its evolution

Our primary goal has been to determine the total FIR luminosity function and subsequently the bolometric luminosity of galaxies

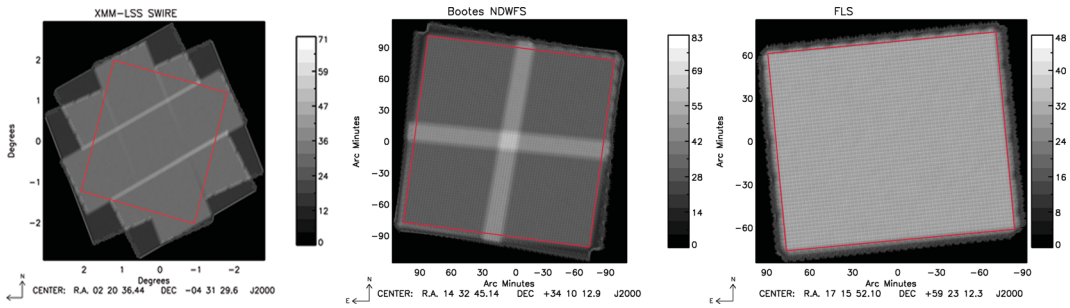

Figure 7. Maps of the number of bolometer samples per pixel in SPIRE 250 μm blank-field observations from Level 6. From the left they are *XMM*-LSS SWIRE (#39), Boötes NDWFS (#37) taken early with conservative overlap and FLS (#40, from SDP). All are parallel mode observations with a nominal coverage of two scans. Overlaps produce a maximum coverage of four scans in *XMM*-LSS SWIRE and eight in Boötes.

Downloaded from http://mnras.oxfordjournals.org/ at NASA Goddard Space Flight Ctr on July 14, 2014

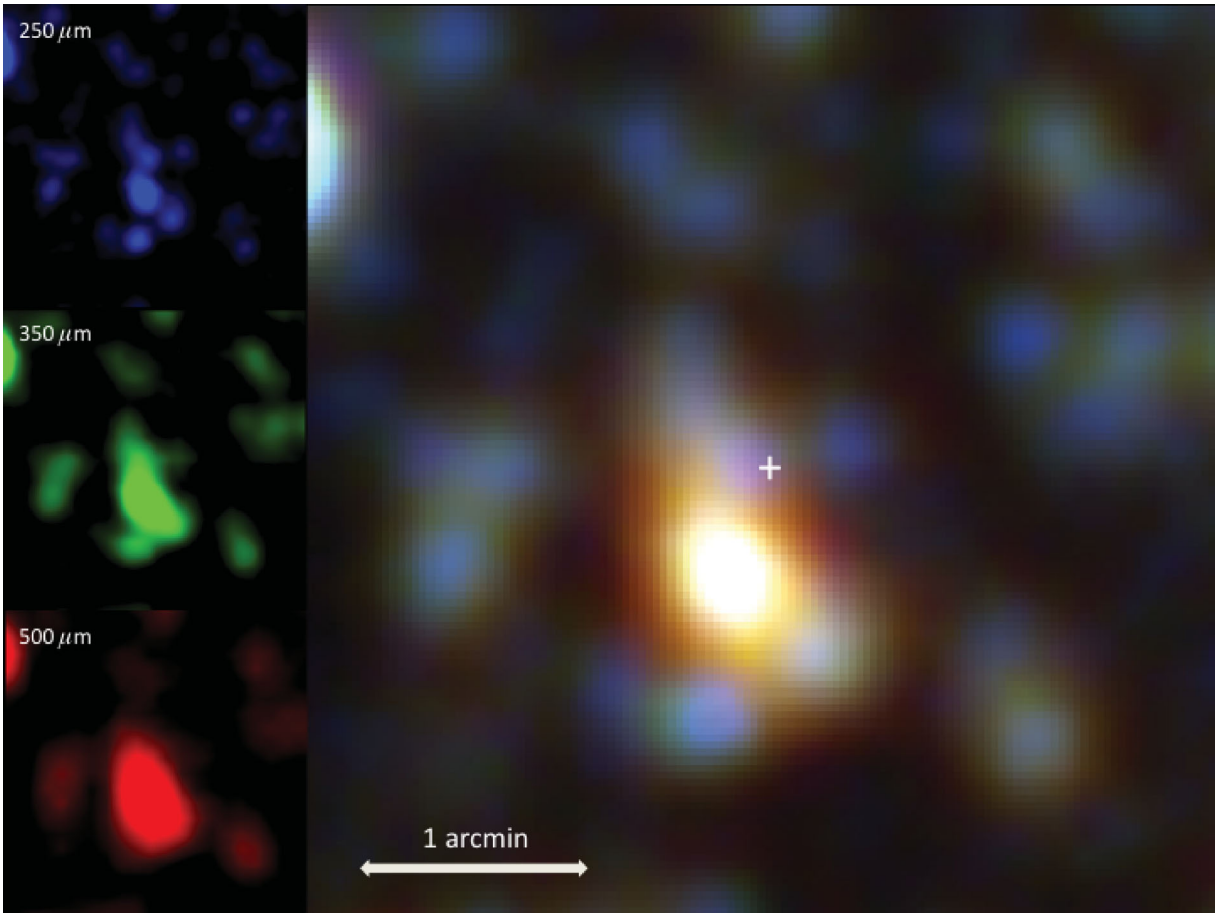

Figure 8. Three-colour *Herschel*-SPIRE image of the central $4 \times 4\,\mathrm{arcmin}^2$ of the galaxy cluster Abell 2218. The left-most panels show the single-band images of the cluster, while the central panel shows a three-colour image generated by resampling the single-band images and their flux scalings to a common pixelization. The centre of the cluster is marked with the cross hairs and a 1 arcmin bar is shown for scaling; north is towards the top of the page. The orange object to the south-east and white object to the south-west of the cluster are images of the multiply imaged submm source studied in detail by, e.g., Kneib et al. (2004); this source has been identified to lie at $z = 2.516$, though due to the complex mass structure of this cluster each image is magnified by a different amount. In the SPIRE bands, this source's integrated flux densities are measured to be 170, 197 and 231 mJy, corresponding to background flux densities of 11.7, 13.5 and 15.4 mJy. The varying colour of the images suggests that different regions of the source galaxy are being imaged to different points in the map. In addition, the known $z = 4.04$ submm source is seen as the pink object just to the east of the cross hairs (Knudsen et al. 2009). The other objects scattered through the image are more typical $z \sim 1$ sources with SEDs peaking shortwards of 250 μm.

over the redshift range $0 < z < 3$. For this analysis, we use galaxies detected in *Herschel* images combined with extensive multi-wavelength data to determine photo-z values where spectroscopic redshifts are not yet available.

Our first results on exploration of the full FIR SED are given by Elbaz et al. (2010), Rowan-Robinson et al. (2010), Hwang et al. (2010) and Chapman et al. (2010). Elbaz et al. (2010) combined photometry from PACS (from the PEP programme) and SPIRE (from HerMES). We found that the total FIR luminosity estimated from extrapolations of *Spitzer* 24 μm data agreed well with direct measurements from *Herschel* at lower redshift but underestimated the power at higher redshifts (as also seen by Nordon et al. 2010). In that work, the longer wavelength (SPIRE) band measurements departed from the model SEDs at lower redshift. This was explored further by Rowan-Robinson et al. (2010), showing that the SPIRE results for some galaxies could be explained with a cold dust component not normally included in canonical templates. Indeed, when simply characterizing the SEDs by their effective dust temperature, we have shown that the SPIRE-detected galaxies cover a broad range of temperatures (Hwang et al. 2010; Magdis et al. 2010) and thus capture warm objects like the 'optically faint radio galaxies' missed by ground-based submm surveys (Chapman et al. 2010).

We have already determined our first measurements of the local luminosity functions at 250, 350 and 500 μm together with a total IR (8–1000 μm) function, finding a local luminosity density of $1.3^{+0.2}_{-0.2} \times 10^8\,\mathrm{L}_\odot\,\mathrm{Mpc}^{-3}$ (Vaccari et al. 2010) and showing that the 250 μm function evolves strongly to $z \sim 1$ (Eales et al. 2010b), similarly to earlier studies at shorter wavelengths. Future analysis (in preparation) will study wider areas with more and better ancillary data and extend these results to higher luminosities, higher redshifts and model the relative contribution of AGN and star formation to the bolometric emission, as well as exploring the relation between the IR luminosities and the stellar properties probed at optical, NIR and UV wavelengths.

3.2.2 *Star formation and environment*

Environment on various scales plays an important role in the process of galaxy formation. Perhaps the most striking observational evidence is that clusters today have a much higher fraction of early-type

Downloaded from http://mnras.oxfordjournals.org/ at NASA Goddard Space Flight Ctr on July 14, 2014

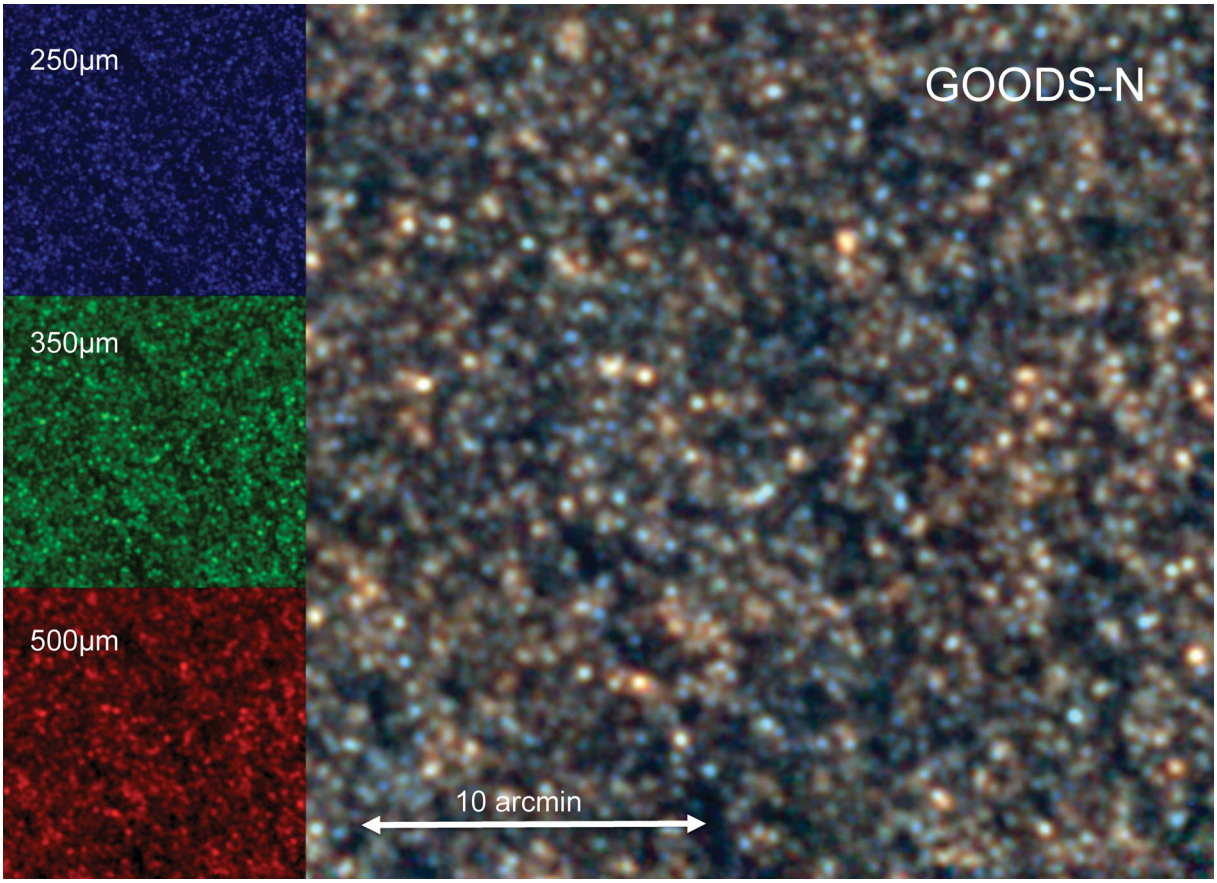

Figure 9. Three-colour *Herschel*-SPIRE image of the GOODS-N region. This is a subset of our GOODS-N observation. The left-most panels show the single-band images of the cluster, while the central panel shows the three-colour image.

Table 6. *Herschel* blank field and cluster lens surveys carried out as Key Programmes or ordinary programmes under Guaranteed Time (GT) or Open Time (OT).

Call	Title	Proposal ID	Time (h)	Reference
Key GT	*Herschel* Extragalactic Multi-tiered Survey (HerMES)	KPGT_soliver_1	806	This paper
Key GT	PACS evolutionary Probe (PEP)	KPGT_dlutz_1	655	Lutz et al., in preparation
Key OT	The Cluster Lensing Survey	KPOT_eegami_1	292	Egami et al. 2010
Key OT	The *Herschel* Astrophysical Terahertz Large Area Survey (H-ATLAS)	KPOT_seales01_2	600	Eales et al. 2010a
Key OT	The Great Observatories Origins Deep Survey (GOODS–*Herschel*)	KPOT_delbaz_1	363	Elbaz et al. 2011
OT1	The *Herschel*–*Akari* NEP Deep Survey	OT1_sserje01_1	74	PI Serjeant
OT1	A deep PACS survey of south	OT1_ttakagi_1	35	PI Takagi
OT1	SPIRE Snapshot Survey of Massive Galaxy Clusters	OT1_eegami	27	Egami et al. (2010)
OT1	Measuring the Epoch of Reionization	OT1_jcarls01_3	79	Carlstrom et al. (2002)
GT2	HerMES Large Mode Survey	GT2_mviero_1	103	Viero et al. (2009) and this paper

galaxies than is found in the field. Likewise, the successful physical models of galaxy formation predict a very strong co-evolution between galaxies and dark matter haloes.

There are many ways of determining the role of environment observationally: one can directly examine the galaxy properties [e.g. the star formation rate (SFR) distribution functions] in different environments; one can explore the environments of galaxies in different luminosity classes; one can use the clustering of particular galaxy populations to infer the mass of the dark matter haloes in which they are located, to relate these to their present-day descendants; or one can directly use the structure in the maps to constrain such models. All these methods have the same basic requirement, a volume sufficiently large to sample enough of the environments of interest, and sufficiently deep to constrain the populations of interest. A simulation in Fig. 12 shows that we could discriminate different halo mass hosts for different subclasses of galaxies and compare the clustering of the FIR galaxies with quasars from optical studies.

First results on the clustering of HerMES galaxies were given by Cooray et al. (2010), indicating that the HerMES sources with $S_{250} > 30$ mJy (at $z \sim 2$) were in dark matter haloes with masses above $(5 \pm 4) \times 10^{12}\,\mathrm{M}_{\odot}$.

Clustering can also be used in other ways. A recent cross-correlation analysis indicates that there is a correlation between

Downloaded from http://mnras.oxfordjournals.org/ at NASA Goddard Space Flight Ctr on July 14, 2014

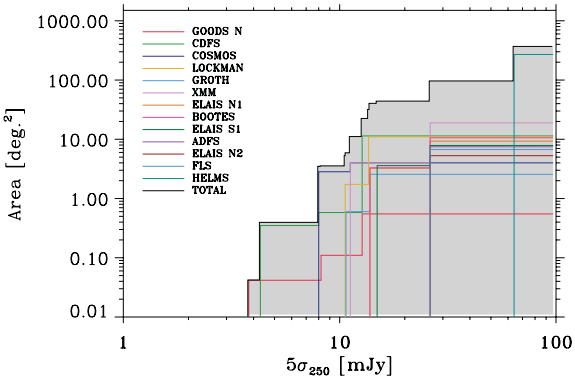

Figure 10. Cumulative area against 5σ instrumental noise level at 250 μm for the HerMES blank-field surveys with SPIRE. The colour coding breaks this down into individual survey fields.

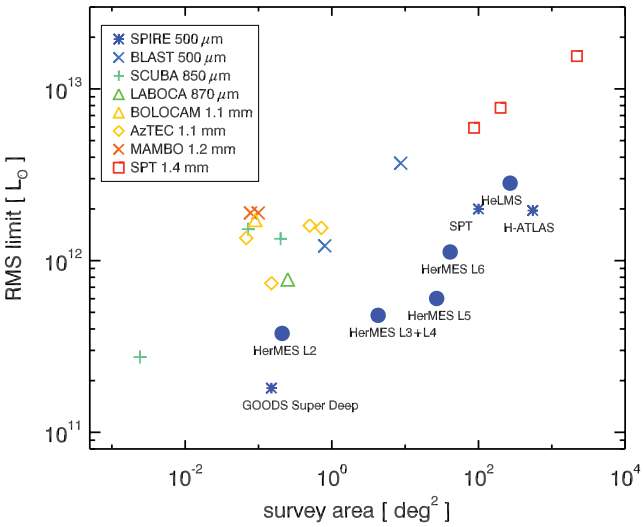

Figure 11. Luminosity limit verses redshift for submm surveys to date. The luminosity limit was calculated assuming a modified blackbody of 35 K at $z = 2$. (References for the points are as follows: SCUBA – Hughes et al. 1998; Scott et al. 2002; Coppin et al. 2006; MAMBO – Greve et al. 2004; Bertoldi et al. 2007; Bolocam – Laurent et al. 2005; AzTEC – Perera et al. 2008; Austermann et al. 2010; Scott et al. 2010b; Aretxaga et al. 2011; LABOCA – Weiß et al. 2009; SPT – Vieira et al. 2010; Williamson et al. 2011; *BLAST* – Devlin et al. 2009, SPT SPIRE – Carlstrom et al. 2002.)

HerMES sources at $z \sim 2$ and foreground galaxies from SDSS at $z \sim 0.2$ and SWIRE at $z \sim 0.4$ (Wang et al. 2011). While some of this signal can be attributed to the intrinsic correlation of galaxies in the overlapping tails of the redshift distributions, there is clear evidence for a signal arising from the amplification of the HerMES source fluxes by lensing from foreground galaxies.

3.2.3 *Extreme galaxies*

Rare objects provide challenges for theories and may expose important but transitory phases in the life cycle of galaxies. The very wide surveys, in particular, will discover many exotic objects, which are prime targets for the Atacama Large Millimeter/Submillimeter Array (ALMA). Galaxies with extremely high SFRs would be difficult to explain with some models of galaxy formation. Limited area submm surveys have already discovered small

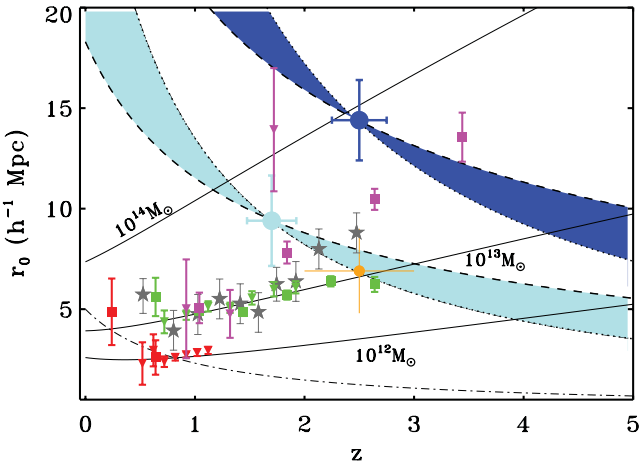

Figure 12. Evolution of comoving correlation length, r_0, with redshift. Solid lines show the predicted clustering amplitude of haloes of given mass. We have simulated data for the clustering of LIRGs (red), ULIRGs (green) and HLIRGs (magenta), assuming they inhabit haloes of mass 10^{12}, 10^{13} and $10^{13.5}$ M$_\odot$, respectively. The simulation is for our 250 μm surveys at Level 5 (square) and Level 6 (triangle). For comparison, we show quasar clustering from Croom et al. (2005) as stars and SCUBA galaxies from Blain et al. (2004) as orange circles. *Spitzer* sources from Farrah et al. (2006) are shown as blue circles, and blue shaded regions extrapolate those objects to their progenitors and descendants.

samples of galaxies with very high SFRs ($\gtrsim$1000 M$_\odot$ yr^{-1}), e.g. SMM J02399−0136 (Ivison et al. 1998), GN20 (Borys et al. 2003; Daddi et al. 2009) and MIPS J142824.0+352619 (Borys et al. 2006). By mapping large areas at the wavelengths where re-emission from star formation peaks, we will be able to quantify the number density of systems of ∼1000 M$_\odot$ yr^{-1} and determine whether there are any systems with even higher SFRs. Even individual examples of such systems would be important as extreme astrophysical laboratories and would provide fruitful targets for new facilities, especially ALMA.

A primary search tool will be the SPIRE colours. Searches have already revealed many galaxies (Schulz et al. 2010) with very red colours $S_{250}/S_{350} < 0.8$ and with flux densities above 50 mJy. These may be a mix of intrinsically cool galaxies at lower redshift, and galaxies at high redshift, including some that are lensed by foreground galaxies.

3.2.4 *Lensed systems*

Lensed systems are interesting because, although lensing is a rare phenomenon, they provide a magnified view of more common, relatively normal, but distant galaxies, which can then be easily studied. An example of a lensed source found in early HerMES data is HERMES J105751.1+573027, a $z = 2.957$ galaxy multiply lensed by a foreground group of galaxies. Coupled with a lensing model derived from high-resolution observations (Gavazzi et al. 2011), the magnification and large image separation allowed us to investigate the continuum SED from the optical to FIR (Conley et al. 2011), as well as model the CO line excitation (Scott et al. 2011) and study the gas dynamics (Riechers et al. 2011).

3.3 Science below the confusion limit

The deepest observations at SPIRE wavelengths suffer substantial confusion noise due to faint unresolved galaxies, and are limited

Downloaded from http://mnras.oxfordjournals.org/ at NASA Goddard Space Flight Ctr on July 14, 2014

in their ability to define true luminosities, SEDs and physical conditions within the most active galaxies during the peak epoch of galaxy formation at redshift $z \sim 2$. We will investigate and employ super-resolution techniques, e.g. CLEAN (Högbom 1974) or matched filtering (Chapin et al. 2011). However, as argued in Oliver (2001), we expect the gains from blind image deconvolution techniques to be modest except at the very highest S/N values.

One approach to combat the problem is to study isolated sources as we have discussed in Elbaz et al. (2010), Brisbin et al. (2010) and Schulz et al. (2010); however, we are pursuing many other mitigating techniques.

3.3.1 *Ultradeep far-infrared galaxy surveys from imaging of rich clusters of galaxies*

Rich clusters can be used as tools to mitigate this effect, allowing high-redshift galaxy formation to be investigated by the gravitational magnification of the primordial galaxies behind the cluster. This has been demonstrated at relevant wavelengths by Smail et al. (2002), Cowie, Barger & Kneib (2002), Metcalfe et al. (2003), Chary, Stern & Eisenhardt (2005) and Swinbank et al. (2010).

Gravitational lensing brightens and separates the images of all background galaxies within 1–2 arcmin of the core of the cluster (e.g. Kneib et al. 2004), making individual background galaxies easier to detect. This also allows the sources of up to about 50 per cent of the otherwise confused and unresolved background radiation to be identified with specific galaxies.

The selected clusters have some of the best archival data available, including deep *HST* Advanced Camera for Surveys/Near Infrared Camera and Multi-Object Spectrometer (NICMOS) images, ultradeep μJy radio imaging, deep MIR imaging from *Spitzer*, and X-ray images from *Chandra*/*XMM–Newton*. The mass and magnification profiles are known accurately, from extensive spectroscopy of multiply lensed images (Kneib et al. 1993).

Our observations of 10 clusters will provide about 180 sources that will allow us to quantify the space density of the faintest *Herschel* galaxies with 10 per cent accuracy. Two clusters (Abell 2218 and Abell 1689) were believed, in advance, to be relatively free of bright lensed galaxies. This was intentional as these were originally intended for very deep observations in order to detect of the order of 10 even fainter lensed sources (to determine the counts of *Herschel* galaxies at the 5-mJy detection level, reaching well below the blank-field confusion limit), so we wanted to avoid confusion from known lensed galaxies. Following modification to our programme in the light of analysis of in-flight data only, Abell 2218 was observed deeper than the others. The results from our SDP cluster observation of Abell 2218 clearly demonstrate that we can detect high-redshift lensed galaxies (see Fig. 8).

3.3.2 *Multicolour one-point fluctuation analysis below the confusion limit*

Analysis of the fluctuations in the cosmic IR background radiation provides unique information on sources too faint to be detected individually (see e.g. Maloney et al. 2005b; Patanchon et al. 2009). Our Level 2 and Level 3 fields allow us to analyse the fluctuation distribution down to flux densities of 2–3 mJy, where much of the background was expected to be resolved. By analysing the fluctuations in all three SPIRE wavebands, we can obtain statistical information on SEDs. This multicolour $P(D)$ analysis provides a powerful method for distinguishing different number count models,

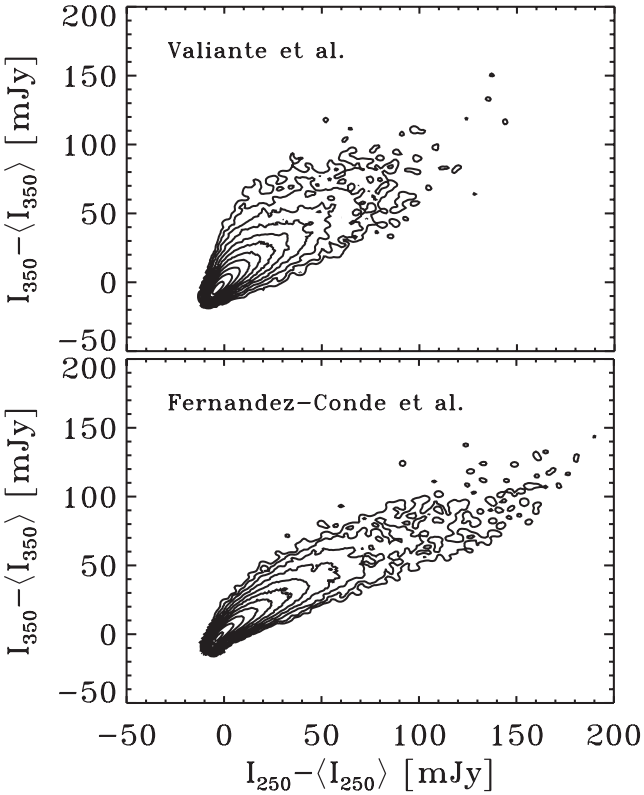

Figure 13. Simulation of a two-dimensional $P(D)$ analysis, showing discrimination between models. The x- and y-axes show the pixel intensities (in mJy beam^{-1}) in the 250 and 350 μm bands, respectively. The contours show the number of pixels with those intensities, logarithmically spaced. The top panel is for the number count model of Valiante et al. (2009), the bottom is for the mock catalogues of Fernandez-Conde et al. (2008) based on the models of Lagache et al. (2003). The simulations are around 10 deg^2 and with 1 mJy of Gaussian noise in each band.

thereby constraining the redshifts and emission properties of the source population (Fig. 13). This requires very precise characterization of the instrument noise for optimal analysis.

We undertook a monochromatic fluctuation analysis using three fields from our SDP data. With that analysis (Glenn et al. 2010), we reached a depth of 2 mJy beam^{-1}, significantly deeper than any previous analysis at these wavelengths. Modelling this distribution with parametrized number counts confirmed the results from resolved sources (Oliver et al. 2010b) and was in disagreement with previous models. The fits accounted for 64, 60 and 43 per cent of the FIR background at 250, 350 and 500 μm, respectively.

3.3.3 *Average SEDs of galaxies contributing to the infrared background*

Prior information from shorter wavelength (e.g. 24 μm with MIPS) can be used to infer the statistical properties (such as source density or SEDs) at longer wavelengths. A more promising route to achieving super-resolution results is to use prior information on the positions of sources from higher resolution data at other wavelengths. This has been demonstrated with HerMES data in Roseboom et al. (2010), achieving robust results for source fluxes down to $S_{250} \approx 10$ mJy.

A related technique is 'stacking', which averages the signal from many similar prior sources. In the absence of significant

Downloaded from http://mnras.oxfordjournals.org/ at NASA Goddard Space Flight Ctr on July 14, 2014

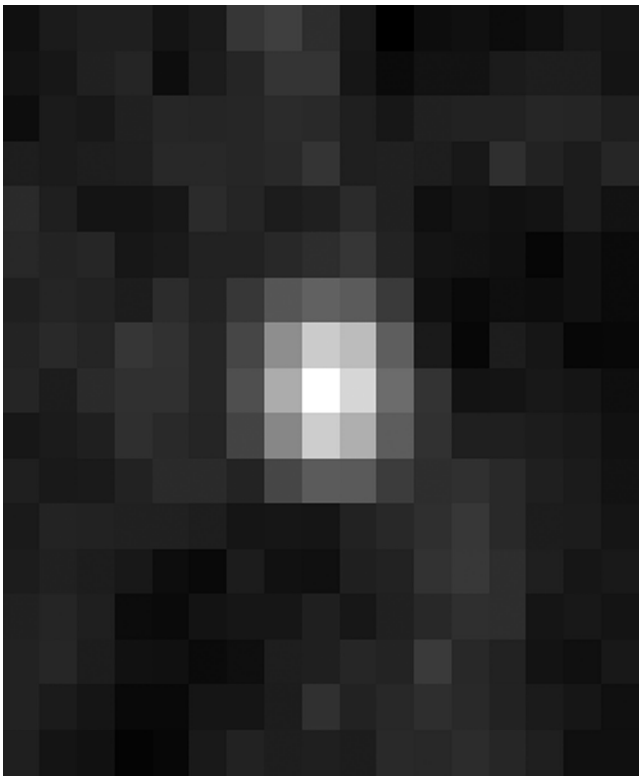

Figure 14. Example of about 4000 *Spitzer* IRAC selected 'bump-3' sources (i.e. objects with peak emission at 5.8 μm) stacked in HerMES SPIRE maps at 250 μm with 6 arcsec pixels. The clear detection allows one to derive aggregate SEDs of this galaxy population, expected to lie at $2.2 < z < 2.8$.

correlations, the confusion variance would then reduce in proportion to the number of prior sources in the 'stack'. Stacking has been successfully applied to *Spitzer* MIPS data; Dole et al. (2006) stacked more than 19 000 24 μm galaxies to find the contributions of the MIR galaxies to the FIR background (70 and 160 μm). With this technique, they gained up to one order of magnitude in depth in the FIR. It appears that a large fraction of the 24 μm sources can be statistically detected at longer wavelengths (e.g. Marsden et al. 2009). Such an analysis applied to *Herschel* will allow us to extend galaxy SEDs to the FIR/submm to quantify the contribution of different populations to the background (e.g. Wang, Cowie & Barger 2006; Dye et al. 2007), or to explore the star formation properties as a function of redshift and stellar mass (e.g. Oliver et al. 2010a). Such procedures might use *Spitzer* 24 μm catalogues and/or the PACS catalogue. This type of analysis is critically dependent on the quality and depth of the ancillary data, and further motivates our choice of very well studied extragalactic fields. An example of this approach is shown in Fig. 14.

Stacking has already been used in some of our analysis (e.g. Ivison et al. 2010; Rigopoulou et al. 2010) and our first results analysing the contribution of various prior populations to the background through stacking will be presented by Vieira et al. (in preparation).

3.3.4 Extragalactic correlations fluctuations

A comprehensive fluctuations analysis is an essential complement to the aspects of our survey allowing us to investigate the majority population of objects, those below the *Herschel* confusion limit. Using the two shallowest tiers of the survey, we can specifically

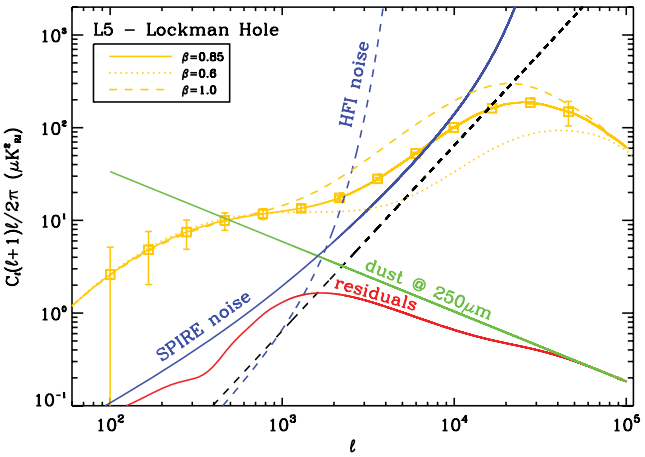

Figure 15. The angular power spectrum of unresolved anisotropies at 350 μm. We model the power spectrum under the halo approach and describe non-linear clustering with a halo occupation number β, as shown by the orange curves. We show simulated binned errors with SPIRE in the 11 deg^2 Lockman Hole L5 field, including both instrument noise and sample variance, and removing shot noise from galaxies below the detection limit (dashed black curve). For reference, the long-dashed and solid blue lines show the noise per multipole for *Planck* and SPIRE, respectively. The green line is the foreground dust spectrum, determined for the same field using dust maps. In red we show the residual foreground spectrum after cleaning with multiwavelength data. Even if not removed, dust does not contaminate small angular scales, where SPIRE excels.

target non-linear clustering on angular scales <10 arcmin, virtually inaccessible to *Planck*, and where SPIRE is not susceptible to low-frequency drifts. The clustering of undetected sources produces fluctuations on larger spatial scales (Haiman & Knox 2000; Knox et al. 2001; Amblard & Cooray 2007) which are expected to be brighter (Scott & White 1999) than Poisson fluctuations on spatial scales >1 arcmin. On large angular scales, background fluctuations measure the linear clustering bias of IR galaxies in dark matter haloes. On small angular scales, fluctuations measure the non-linear clustering within individual dark matter haloes, and the physics governing how FIR galaxies form within a halo as captured by the occupation number of FIR sources. This halo approach (e.g. Cooray & Sheth 2002) will allow us to compare the results of a *Herschel* fluctuations survey with studies at other wavelengths, to obtain a consistent picture of galaxy clustering and evolution. Finally, this fluctuation survey is designed to complement surveys by *Planck* on larger angular scales (see Fig. 15).

First measurements of correlated fluctuations from clustered IR galaxies at submm wavelengths have been detected by Lagache et al. (2007), Grossan & Smoot (2007), Viero et al. (2009), Hall et al. (2010), Dunkley et al. (2010) and Hajian et al. (2011). Our first results (Amblard et al. 2011) have extended these findings at arcminute scales by measuring the non-linear one-halo component for the first time. Modelling suggests that at 350 μm 90 per cent of the background intensity is generated by faint galaxies at $z > 1$ in dark matter haloes with a minimum mass of $\log[M_{\rm min}/{\rm M}_\odot] = 11.5^{+0.7}_{-0.2}$, in agreement with *BLAST* (Viero et al. 2009).

3.4 Additional science enabled by HerMES

We expect to detect over 100 000 sources in our survey. The scientific themes explored in Sections 3.2 and 3.3 will be dramatically extended and improved with the samples available now and the full sample once complete. Here we mention briefly a very few other

Downloaded from http://mnras.oxfordjournals.org/ at NASA Goddard Space Flight Ctr on July 14, 2014

science topics that might be addressed by us or others using such a large survey.

The FIR colours of the *Herschel* sources can help in addressing the question of how much of the energy production comes from accretion (AGN) and how much from star formation. First results on an SDSS sample of AGN (Hatziminaoglou et al. 2010) find that one-third are detected by SPIRE, with the long wavelength colours indistinguishable from star-forming galaxies. Modelling of the full SED required the combined contribution of both AGN and starburst components, with the former dominating the emission at the MIR wavelengths and the latter contributing mostly to the FIR wavelengths. This suggests that SPIRE detects the star formation in AGN, with little contamination from any dusty torus, offering high hopes for disentangling nuclear and star formation activity.

The wealth of data in these fields means we can explore the FIR properties of many known samples. Our first results on Lyman break galaxies have already shown that we can detect U-band drop-out sources with stacking (Rigopoulou et al. 2010) and far-UV drop-out sources individually (Burgarella 2011). We have also shown that galaxies selected on the basis of the *Spitzer* Infrared Array Camera (IRAC) colours probe a wide range of FIR temperatures (Magdis et al. 2010).

We will compare the FIR measure of star formation with other tracers. In collaboration with the PEP team, we examined the well-known FIR radio correlation in GOODS-N (Ivison et al. 2010). Exploring $q_{\rm IR}$, i.e. the logarithmic ratio of the rest-frame 8–1000 μm flux to the 1.4-GHz flux density, there is no evidence that $q_{\rm IR}$ changes significantly for the whole sample: $q_{\rm IR} \propto (1+z)^{\gamma}$, where $\gamma = -0.04 \pm 0.03$ at $z = 0$–2, although if the small volume at $z < 0.5$ is removed we find $\gamma = -0.26 \pm 0.07$. HerMES will create a complete data set to understand the global relationship between FIR and optical galaxies, the effect of dust attenuation in optical/UV populations, and phenomena in individual galaxies. First results comparing HerMES and *GALEX* (Buat et al. 2010) confirm that total IR luminosity accounts for 90 per cent of the total SFR, though this reduces to 70 per cent when considering the lower SFR systems ($\dot{M}_* < 1\,{\rm M}_\odot\,{\rm yr}^{-1}$).

These ancillary data can also be used to investigate the detailed properties of the FIR galaxies, e.g. their morphology. One study has explored galaxies with morphological classifications at $2 < z < 3$ and shows that the mean SFR for the spheroidal galaxies is about a factor of 3 lower than for the disc-like galaxies (Cava et al. 2010).

Observations of the rich clusters – the densest known regions of the Universe – yield information about their astrophysics and history via the Sunyaev-Zel'dovich (SZ) effect (Birkinshaw 1999; Carlstrom, Holder & Reese 2002), which dominates the extended several-arcmin-scale emission of clusters at wavelengths longer than about 500 μm. The SZ effect arises from inverse-Compton scattering of cosmic microwave background photons by hot (1–10 keV) gas in the intracluster medium. We intend to combine SPIRE and *Planck* data to measure the SZ effect and the submm foregrounds between 150 GHz and 1 THz. Based on the different spectral shapes of the SZ effect and foregrounds, SPIRE data will enable us to separate out Galactic dust, cluster and background galaxies, the thermal SZ effect and the effects of relativistic electrons.

4 DATA PRODUCTS

4.1 SPIRE catalogues

As an illustration of the kind of data products that HerMES will produce, we show an approximation to the SPIRE 250 μm survey areas and depths in Table 7 [together with The *Herschel* Astrophysical Terahertz Large Area Survey (H-ATLAS) and H-GOODS]. We indicate an estimate of the numbers of galaxies on the sky from the Valiante et al. (2009) model, which is one of the best fits to the current data and to a direct determination of the counts from both resolved sources (Oliver et al. 2010b) and fluctuation analyses (Glenn et al. 2010). Finally, we give an estimate of the numbers of catalogued sources above those flux density limits estimated from our 24 μm driven extractions (at deep levels) and our single-band detections at shallow levels. Overall, we thus expect 100 000 sources detected at $>5\sigma$.

Table 7. Projected SPIRE survey results for the 250 μm band. This table simplifies the survey giving approximate instrumental noises in four tiers (L1 includes GOODS-N). The 5σ confusion noise from Nguyen et al. (2010) is 29 mJy, approximately the Level 6 depth. Numbers of 250 μm sources are estimated from a count model (Valiante et al. 2009, $N_{\rm Val}$), our $P(D)$ analysis (Glenn et al. 2010, $N_{\rm Glenn}$) and from our raw number counts in fields that we have at these depths, extracted as described in Smith et al. (2011, $N_{\rm cat}$).

Levels	Area (deg^2)	$5\sigma_{250}$ (mJy)	$N_{\rm Val}$ (10^3)	$N_{\rm Glenn}$ (10^3)	$N_{\rm cat}$ (10^3)
PACS Ul.	0.012				
Level 1	0.15	4	2.2	2.0 ± 0.1	–
Levels 2–4	6.0	10	17	22.4 ± 0.9	
Level 5	37	15	53	73.6 ± 2.3	52
Level 6	52	26	20	28.1 ± 0.6	30
H-ATLAS	570	45	76	90.6 ± 2.9	115
Level 7 (HeLMS)	270	64	130		24

4.2 Ancillary Data

4.2.1 *Required ancillary data*

To estimate the required ancillary data, we have examined our first cross-identified catalogues (Roseboom et al. 2010). These are lists with photometry at the positions of known 24 μm galaxies and thus are not a complete description of the *Herschel* populations; however, they are approximately 90 per cent complete.

In Fig. 16, we show the number of sources as a function of 250 μm flux and i- or $K_{\rm s}$-band magnitude. Table 8 presents the estimated depth required to detect SPIRE galaxies from simulated catalogues from the model of Xu et al. (2003).

4.2.2 *Available ancillary data*

The survey fields are very well studied and it is outside the scope of this paper to provide a complete description of all the many ancillary data that are available in these fields. A more detailed description of the ancillary data will be provided by Vaccari et al. (in preparation). Our intention is to homogenize and make publicly available all ancillary/complementary data in our final data release.

4.2.3 *Deliverable data products*

Our intended data products are summarized in Table 9. The *Herschel* source catalogues from SPIRE and PACS data (SCAT and PCAT, respectively) will consist of the usual independent lists where sources are selected from data at one wavelength without reference to any other. Associated with these catalogues will be validation analyses, including completeness, reliability and the information necessary

Downloaded from http://mnras.oxfordjournals.org/ at NASA Goddard Space Flight Ctr on July 14, 2014

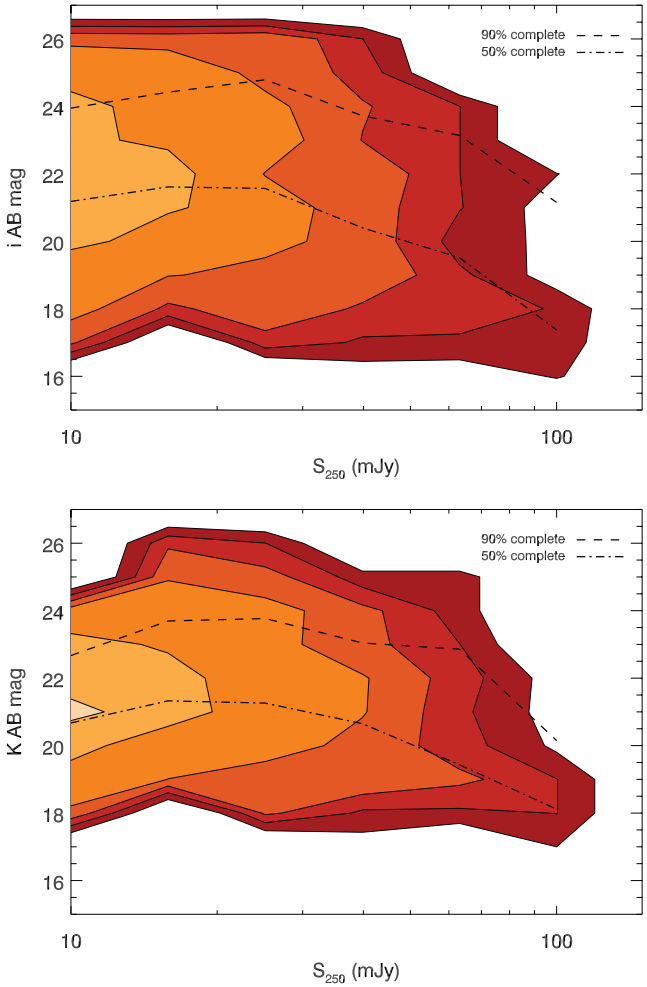

Figure 16. Density of SPIRE sources as a function of 250 μm flux density and optical, *i*-band (top) and K_s-band (bottom) magnitudes. The dashed line indicates the optical or NIR depth required to detect 90 per cent of the sample at a given 250 μm flux density, while the dot–dashed lines is the depth to detect 10 per cent.

to construct selection functions for standard scientific analysis. In addition, these products will include fluxes estimated for sources from other catalogues (including sources from public *Spitzer* catalogues). Our first SCAT products are described in Smith et al. (2011) and our first PCAT products by Aussel et al. (in preparation).

The SPCAT product will include all *Herschel* bands. Upper limits will be listed for sources detected in some *Herschel* bands but not others.

The XID product will include associations with a variety of large homogenous catalogues, including, but not necessarily limited to, public *Spitzer* catalogues. Our first XID products are described by Roseboom et al. (2010).

Maps from SPIRE and PACS data (SMAP and PMAP, respectively) will be suitable for extended source analysis, fluctuation analysis, etc. Our first SMAP products are described by Levenson et al. (2010).

4.2.4 Other data products

We expect to produce additional data products as an output of the pursuit of our science goals. These will include maps and catalogues of sources from data acquired at other facilities (optical, NIR, radio, etc.). It will also include value-added products where observed data have been used to model other properties of the catalogued objects, such as photometric redshift, luminosity or spectral class. It is impossible to define a complete list of such products at this stage. We will make these available to the community on a best-efforts basis.

Table 8. Estimates of depth required to detect SPIRE galaxies at various other wavelengths. The estimates are based on the mock catalogues of Xu et al. (2003) cut to have $S_{250} > 30$ mJy. We tabulate the depth at which a given percentage of the catalogue would be detected.

Band	Units	10 per cent	50 per cent	90 per cent
UV(0.2 Å)	AB	22.0	28.3	33.7
R	AB	18.6	22.5	25.2
I	AB	18.1	21.5	23.6
K	AB	17.2	19.5	20.8
3.6 μm	μJy	380	90	30
24 μm	μJy	3000	880	220
70 μm	mJy	42	13	4.7
850 μm	mJy	6.8	2.3	1.1
21 cm	μJy	330	100	50

4.2.5 Simulated data

In order to plan our surveys and simulate our expectations, we have compiled and homogenized mock catalogues from these and other models, which are publicly available via hermes.sussex.ac.uk/. These and other simulations will be made available on a best-efforts basis through this site.

4.2.6 Data release schedule

Early data release: EDR. Our first data release was proposed to be in time for the second open call for *Herschel* proposals (OT2). This was before the SDP release rules were established and when OT2 was expected to be earlier. In fact, our SDP Early Data Release was made on 2010 July 1. This meant it was in time for OT1 (due on 2010 July 22). This data release is described in Smith et al. (2011) and, as we proposed, it was restricted to SPIRE high S/N sources in order to be as reliable as possible. It included maps from our Abell 2218 observation (#1) and 250 μm catalogues limited at $S_{250} > 100$ mJy for all our SDP fields [First Look Survey (FLS) #40, GOODS-N #14, Lockman-SWIRE #28, Lockman-North #19].

A second Early Data Release EDR2 was made on 2011 September 19 which included bright source catalogues similar to those for EDR but for the Data Release 1 (DR1) fields (see Table 1).

Data Release 1: DR1. An extensive Data Release (DR1) of maps and catalogues will be made on 2012 March 27. DR1 will include data from the SDP observations and all SPIRE observations completed by 2010 May 1 [A2219 #7, MS 0451.6−0305 #3, ECDFS #15, *XMM*-LSS #36, Extended Groth Strip (EGS) HerMES #29, Groth Strip #17, Boötes #37, ADFS #38, ELAIS N1 HerMES #31]. All products will be accompanied by documentation in the form of papers in refereed journals.

Data Release 2: DR2. DR2 will occur at the end of the mission. This will include all our deliverable data products and ancillary data in their final form.

Downloaded from http://mnras.oxfordjournals.org/ at NASA Goddard Space Flight Ctr on July 14, 2014

Table 9. Deliverable data products.

Name	Description	Minimum parameters
SCAT	SPIRE source catalogues	Positions, fluxes, errors, S/N values, etc.
SMAP	SPIRE maps	Maps of flux, noise and coverage
PCAT	PACS source catalogues	Positions, fluxes, errors, S/N values, etc.
PMAP	PACS maps	Maps of flux, noise and coverage
SPCAT	SPIRE/PACS band-merged catalogues	Positions, fluxes, errors, S/N values, etc.
CLUS	Catalogues and maps for clusters	As above for maps and catalogues
XID	Cross-identifications with selected homogenous catalogues at other wavelengths.	Fluxes, errors, S/N values, positions, positional offsets

4.3 Archival value and data access

As our observations are in all the most well-studied survey fields, the legacy value is enormous. We fully expect a rich data base, leading to abundant science beyond the resources of our team. In addition to any ESA data releases (herschel.esac.esa.int/), our data will be released through the *Herschel* Database in Marseille, HeDaM (hedam.oamp.fr/HerMES). The information system design and its implementation are developed under the SITOOLS middleware interface provided by the Centre National des Etudes Spatiales (CNES) (vds.cnes.fr/sitools/). The data (images and catalogues) are accessible in various formats (FITS files, VOTable, ASCII) and accessible through Virtual Observatory Tools. Advanced searches, cross-correlated data and the corresponding images are also implemented, including visualization facilities like ALADIN (http://aladin.u-strasbg.fr/) and TOPCAT (http://www.star.bris.ac.uk/~mbt/topcat/).

5 DISCUSSION AND CONCLUSION

We have presented the HerMES. This survey builds on the legacy of existing FIR and submm surveys. It will provide a census of star formation activity over the wavelengths where the obscured star formation peaks and over representative volumes (and thus environments) of the Universe at different epochs. It is being carried out in some of the best-studied extragalactic fields on the sky, which is invaluable for the interpretation of the data both technically, by enabling accurate identifications and reducing the impact of confusion noise, and scientifically, by allowing exploration of the physical processes manifest at different wavelengths. We have provided the description and rationale of the survey design. We also described the data products we plan to deliver and their schedule.

Our first results from the SDP data have fully demonstrated the promise of the full survey. We have quantified the confusion noise at SPIRE wavelengths (Nguyen et al. 2010), $5\sigma_{250} = 29.0 \pm 1.5$ mJy, finding it to be very similar to what was anticipated. This confusion is challenging to deal with (e.g. Brisbin et al. 2010) but we are exploring sophisticated techniques to deal with this (e.g. through prior positional information; Roseboom et al. 2010), and using $P(D)$ analysis have already probed to 4 mJy and accounted for 64 per cent of the background at 250 μm (Glenn et al. 2010). It seems that previous phenomenological galaxy populations need revision (Glenn et al. 2010; Oliver et al. 2010b), and we now anticipate that we will be able to catalogue over 100 000 galaxies with $>5\sigma$ detections at 250 μm. The galaxies appear to be the luminous actively star-forming galaxies we expected (e.g. Elbaz et al. 2010) with a strongly evolving luminosity function (Eales et al. 2010b; Vaccari et al. 2010). Also, as expected, SPIRE probes a wide range of effective temperatures, including warm galaxies and those cooler galaxies typically seen by submm surveys (Chapman et al. 2010; Hwang et al. 2010; Magdis et al. 2010; Roseboom et al. 2011). A clue to the problems that the phenomenological models have may lie in the hints of the presence of cooler than expected dust in some galaxies (Rowan-Robinson et al. 2010; Schulz et al. 2010). We also see evidence for sources being magnified through gravitational lensing by foreground galaxies in the field (Schulz et al. 2010; Conley et al. 2011; Wang et al. 2011) and in targeted clusters. These magnified galaxies provide a window to study intrinsically lower luminosity galaxies at higher redshifts. We have identified strong clustering of SPIRE galaxies (e.g. Cooray et al. 2010; Amblard et al. 2011), indicating that these luminous systems lie in massive dark matter haloes and implying they are the progenitors of galaxies in rich groups and clusters today, i.e. elliptical galaxies.

HerMES will constitute a lasting legacy to the community, providing an essential complement to multiwavelength surveys in the same fields and providing targets for follow-up using many facilities, e.g. ALMA. The results are expected to provide an important benchmark for theoretical models of galaxy evolution for the foreseeable future.

ACKNOWLEDGMENTS

We acknowledge support from the UK Science and Technology Facilities Council, grant numbers ST/F002858/1 and ST/I000976/1. HCSS/HSPOT/HIPE are joint developments by the Herschel Science Ground Segment Consortium, consisting of ESA, the NASA Herschel Science Center and the HIFI, PACS and SPIRE consortia.

SPIRE has been developed by a consortium of institutes led by Cardiff University (UK) and including University of Lethbridge (Canada), NAOC (China), CEA, LAM (France), IFSI, University of Padua (Italy), IAC (Spain), Stockholm Observatory (Sweden), Imperial College London, RAL, UCL-MSSL, UKATC, University of Sussex (UK) and Caltech, JPL, NHSC, University of Colorado (USA). This development has been supported by national funding agencies: CSA (Canada); NAOC (China); CEA, CNES, CNRS (France); ASI (Italy); MCINN (Spain); SNSB (Sweden); STFC, UKSA (UK) and NASA (USA).

REFERENCES

Amblard A., Cooray A., 2007, ApJ, 670, 903
Amblard A. et al., 2011, Nat, 470, 510
Aretxaga I. et al., 2011, MNRAS, 415, 3831
Austermann J. E. et al., 2010, MNRAS, 401, 160
Baugh C. M., Lacey C. G., Frenk C. S., Granato G. L., Silva L., Bressan A., Benson A. J., Cole S., 2005, MNRAS, 356, 1191
Berta S. et al., 2011, A&A, 532, 49
Bertoldi F. et al., 2007, ApJS, 172, 132
Birkinshaw M., 1999, Phys. Rep., 310, 97

Downloaded from http://mnras.oxfordjournals.org/ at NASA Goddard Space Flight Ctr on July 14, 2014

Blain A. W., Chapman S. C., Smail I., Ivison R., 2004, ApJ, 611, 725
Bonfield D. G., Jarvis M. J., Consortium V., 2010, BAAS, 36, 1127
Borys C., Chapman S., Halpern M., Scott D., 2003, MNRAS, 344, 385
Borys C. et al., 2006, ApJ, 636, 134
Brisbin D. et al., 2010, MNRAS, 409, 66
Buat V. et al., 2010, MNRAS, 409, L1
Burgarella D. et al., 2011, ApJ, 734, 12
Carlstrom J. E., Holder G. P., Reese E. D., 2002, ARA&A, 40, 643
Cava A. et al., 2010, MNRAS, 409, L19
Chapin E. L. et al., 2011, MNRAS, 411, 505
Chapman S. C. et al., 2010, MNRAS, 409, L13
Chary R., Stern D., Eisenhardt P., 2005, ApJ, 635, L5
Clements D. L., Bendo G., Pearson C., Khan S. A., Matsuura S., Shirahata M., 2011, MNRAS, 411, 373
Conley A. et al., 2011, ApJ, 732, L35
Cooray A., Sheth R., 2002, Phys. Rep., 372, 1
Cooray A. et al., 2010, A&A, 518, L22
Coppin K. et al., 2006, MNRAS, 372, 1621
Cowie L. L., Barger A. J., Kneib J., 2002, AJ, 123, 2197
Croom S. M. et al., 2005, MNRAS, 356, 415
Daddi E. et al., 2009, ApJ, 694, 1517
Devlin M. J. et al., 2009, Nat, 458, 737
Dickinson M., FIDEL team, 2007, BAAS, 38, 822
Dickinson M., Giavalisco M., GOODS Team, 2003, in Bender R., Renzini A., eds, The Mass of Galaxies at Low and High Redshift. Springer-Verlag, Berlin, p. 324
Dole H. et al., 2006, A&A, 451, 417
Dunkley J. et al., 2010, ApJ, 739, 52
Dunlop J. S. et al., 2004, MNRAS, 350, 769
Dunlop J. et al., 2007, in *Spitzer* Proposal ID #40021
Dye S., Eales S. A., Ashby M. L. N., Huang J., Egami E., Brodwin M., Lilly S., Webb T., 2007, MNRAS, 375, 725
Eales S., Lilly S., Gear W., Dunne L., Bond J. R., Hammer F., Le Fèvre O., Crampton D., 1999, ApJ, 515, 518
Eales S. et al., 2010a, PASP, 122, 499
Eales S. A. et al., 2010b, A&A, 518, L23
Egami E. et al., 2010, A&A, 518, L12
Elbaz D. et al., 1999, in Cox P., Kessler M., eds, ESA Special Publ. Vol. 427, The Universe as Seen by ISO. ESA, Noordwijk, p. 999
Elbaz D. et al., 2010, A&A, 518, L29
Elbaz D. et al., 2011, A&A, 533, 119
Fadda D. et al., 2006, AJ, 131, 2859
Farrah D. et al., 2006, ApJ, 641, L17
Fernandez-Conde N., Lagache G., Puget J., Dole H., 2008, A&A, 481, 885
Fixsen D. J., Dwek E., Mather J. C., Bennett C. L., Shafer R. A., 1998, ApJ, 508, 123
Franceschini A., Rodighiero G., Vaccari M., Berta S., Marchetti L., Mainetti G., 2010, A&A, 517, A74
Frayer D. T. et al., 2009, AJ, 138, 1261
Gavazzi R. et al., 2011, ApJ, 738, 125
Giacconi R. et al., 2001, ApJ, 551, 624
Glenn J. et al., 2010, MNRAS, 409, 109
Greve T. R., Ivison R. J., Bertoldi F., Stevens J. A., Dunlop J. S., Lutz D., Carilli C. L., 2004, MNRAS, 354, 779
Greve T. R., Pope A., Scott D., Ivison R. J., Borys C., Conselice C. J., Bertoldi F., 2008, MNRAS, 389, 1489
Griffin M. J. et al., 2010, A&A, 518, L3
Grossan B., Smoot G. F., 2007, A&A, 474, 731
Haiman Z., Knox L., 2000, ApJ, 530, 124
Hajian A. et al., 2011, ApJ, 530, 124
Hall N. R. et al., 2010, ApJ, 718, 632
Hatziminaoglou E. et al., 2010, A&A, 518, L33
Högbom J. A., 1974, A&AS, 15, 417
Hughes D. H. et al., 1998, Nat, 394, 241
Hwang H. S. et al., 2010, MNRAS, 409, 75
Ivison R. J., Smail I., Le Borgne J., Blain A. W., Kneib J., Bezecourt J., Kerr T. H., Davies J. K., 1998, MNRAS, 298, 583
Ivison R. J. et al., 2010, A&A, 518, L31
Jannuzi B. T., Dey A., 1999, in Weymann R., Storrie-Lombardi L., Sawicki M., Brunner R., eds, ASP Conf. Ser. Vol. 191, Photometric Redshifts and the Detection of High Redshift Galaxies. Astron. Soc. Pac., San Francisco, p. 111
Khan S. A. et al., 2007, ApJ, 665, 973
Kneib J. P., Mellier Y., Fort B., Mathez G., 1993, A&A, 273, 367
Kneib J., van der Werf P. P., Kraiberg Knudsen K., Smail I., Blain A., Frayer D., Barnard V., Ivison R., 2004, MNRAS, 349, 1211
Knox L., Cooray A., Eisenstein D., Haiman Z., 2001, ApJ, 550, 7
Knudsen K. K., Neri R., Kneib J., van der Werf P. P., 2009, A&A, 496, 45
Lacy M., SERVS team, 2009, BAAS, 41, 671
Lagache G., Puget J., Gispert R., 1999, Ap&SS, 269, 263
Lagache G., Dole H., Puget J., 2003, MNRAS, 338, 555
Lagache G., Bavouzet N., Fernandez-Conde N., Ponthieu N., Rodet T., Dole H., Miville-Deschênes M., Puget J., 2007, ApJ, 665, L89
Laurent G. T. et al., 2005, ApJ, 623, 742
Lawrence A. et al., 2007, MNRAS, 379, 1599
Le Borgne D., Elbaz D., Ocvirk P., Pichon C., 2009, A&A, 504, 727
Le Fèvre O. et al., 2005, A&A, 439, 845
Le Floc'h E. et al., 2005, ApJ, 632, 169
Levenson L. et al., 2010, MNRAS, 409, 83
Lockman F. J., Jahoda K., McCammon D., 1986, ApJ, 302, 432
Lonsdale C. J. et al., 2003, PASP, 115, 897
Lutz D. et al., 2011, A&A, 532, 90
Magdis G. E. et al., 2010, MNRAS, 409, 22
Maloney P. R. et al., 2005a, ApJ, 635, 1044
Maloney P. R. et al., 2005b, ApJ, 635, 1044
Marsden G. et al., 2009, ApJ, 707, 1729
Matsuura S. et al., 2010, ApJ, 737, 2
Metcalfe L. et al., 2003, A&A, 407, 791
Mo H. J., White S. D. M., 2002, MNRAS, 336, 112
Nguyen H. T. et al., 2010, A&A, 518, L5
Nordon R. et al., 2010, A&A, 518, L24
Oliver S. J., 2001, in Pilbratt G. L., Cernicharo J., Heras A. M., Prusti T., Harris R., eds, ESA Special Publ. Vol. 460, The Promise of the Herschel Space Observatory. ESA, Noordwijk, p. 105
Oliver S. J., Rowan-Robinson M., Saunders W., 1992, MNRAS, 256, 15P
Oliver S. et al., 2000, MNRAS, 316, 749
Oliver S. et al., 2002, MNRAS, 332, 536
Oliver S. et al., 2010a, MNRAS, 405, 2279
Oliver S. J. et al., 2010b, A&A, 518, L21
Owen F. N., Morrison G. E., 2008, AJ, 136, 1889
Patanchon G. et al., 2009, ApJ, 707, 1750
Pearson C., Khan S. A., 2009, MNRAS, 399, L11
Perera T. A. et al., 2008, MNRAS, 391, 1227
Pierre M. et al., 2006, MNRAS, 372, 591
Pilbratt G. L. et al., 2010, A&A, 518, L1
Poglitsch A. et al., 2010, A&A, 518, L2
Puget J., Abergel A., Bernard J., Boulanger F., Burton W. B., Desert F., Hartmann D., 1996, A&A, 308, L5
Riechers D. A. et al., 2011, ApJ, 733, L12
Rigopoulou D. et al., 2010, MNRAS, 409, L7
Roseboom I. G. et al., 2010, MNRAS, 409, 48
Roseboom I. et al., 2012, MNRAS, 419, 2758
Rowan-Robinson M. et al., 2010, MNRAS, 409, 2
Sanders D. B. et al., 2007, ApJS, 172, 86
Scoville N. et al., 2007, ApJS, 172, 1
Saunders W., 1990, PhD thesis, Queen Mary College, Univ. London
Schlegel D. J., Finkbeiner D. P., Davis M., 1998, ApJ, 500, 525
Schulz B. et al., 2010, A&A, 518, L32
Scott D., White M., 1999, A&A, 346, 1
Scott S. E. et al., 2002, MNRAS, 331, 817
Scott K. S. et al., 2010a, ApJS, 191, 212
Scott K. S. et al., 2010b, MNRAS, 405, 2260
Scott K. S. et al., 2011, ApJ, 733, 29
Shupe D. L. et al., 2008, AJ, 135, 1050
Smail I., Ivison R. J., Blain A. W., 1997, ApJ, 490, L5
Smail I., Ivison R. J., Blain A. W., Kneib J., 2002, MNRAS, 331, 495

Downloaded from http://mnras.oxfordjournals.org/ at NASA Goddard Space Flight Ctr on July 14, 2014

Smith A. J. et al., 2012, MNRAS, 419, 377
Spergel D. N. et al., 2003, ApJS, 148, 175
Springel V., Frenk C. S., White S. D. M., 2006, Nat, 440, 1137
Swinbank A. M. et al., 2010, Nat, 464, 733
Vaccari M. et al., 2010, A&A, 518, L20
Valiante E., Lutz D., Sturm E., Genzel R., Chapin E. L., 2009, ApJ, 701, 1814
Vieira J. D. et al., 2010, ApJ, 719, 763
Viero M. P. et al., 2009, ApJ, 707, 1766
Wang W., Cowie L. L., Barger A. J., 2006, ApJ, 647, 74
Wang L. et al., 2011, MNRAS, 414, 596
Weiß A. et al., 2009, ApJ, 707, 1201
Williamson R. et al., 2011, ApJ, 738, 139
Xu C. K., Lonsdale C. J., Shupe D. L., Franceschini A., Martin C., Schiminovich D., 2003, ApJ, 587, 90

APPENDIX A: DETAILED RATIONALE FOR DEFINITION OF EACH SURVEY REGION

Our deepest tier, Level 1 (#13), covers the GOODS-South (GOODS-S) region, which is one of the two deepest *Spitzer* fields (Dickinson, Giavalisco & GOODS Team 2003).

The other GOODS field, GOODS-N, is covered by one of our Level 2 observations (#14), though our observations are substantially wider. The boundaries of our other Level 2 field, the Extended *Chandra Deep Field*-South field (ECDFS, #15), is defined by the deep For-Infrared Deep Extragalatic Legacy (FIDEL) survey coverage (Dickinson & FIDEL team 2007).

Our EGS field at Level 3 (#17) is also defined to match the FIDEL boundaries. The Lockman-East field at Level 3 (#18, #18B) covers *Spitzer* guaranteed time programme data (#18) and the *Spitzer* Legacy programme of Egami et al. (2010, #18B). Those deep sets (#13, 14, 15, 17 and 18) were all coordinated with the PEP (Lutz et al., in preparation) team. The Lockman-North field at Level 3 (#19, 20) covers the deep *Spitzer* field defined, e.g., in Owen & Morrison (2008).

The UDS field at Level 4 (#23) is defined by the *Spitzer* SpUDS observations (Dunlop et al. 2007) and we observe this field at Level 3 (#21) with PACS. The *Spitzer* COSMOS (Sanders et al. 2007) field is observed in #22 and #22B, though our principal definition was the PEP observation of this field (discussed more in Section 2.8). The VVDS field at Level 4 (#24, 26) is not defined by *Spitzer* observations but by the optical spectroscopic survey of Le Fèvre et al. (2005).

The Level 5 and 6 fields, CDFS SWIRE, Lockman SWIRE, *XMM*-LSS SWIRE, ELAIS N1 SWIRE, ELAIS N2 SWIRE (#27, 28, 34–36, 39 and 41), are defined by the Spitzer Wide Area Infrared Survey (SWIRE) fields (Lonsdale et al. 2003) – those fields based in turn on the European Large Area *ISO* survey, ELAIS (Oliver et al. 2000), the *XMM*-LSS survey (Pierre et al. 2006) and flanking the ECDFS (Giacconi et al. 2001) and various Lockman Hole fields (Lockman, Jahoda & McCammon 1986). The Boötes NOAO Deep Wide-Field Survey (NDWFS) field at Level 6 (#37) is defined by the *Spitzer* Guaranteed time survey (Jannuzi & Dey 1999). The FLS field Level 6 (#40) is defined by the extragalactic part of the *Spitzer* FLS (Fadda et al. 2006) and is commonly referred to now as XFLS. The ADFS (#38) is defined with reference to the *Spitzer* (Scott et al. 2010a; Clements et al. 2011) and *BLAST* observations (but see Section 2.8). The Level 5 observations in #29, 30, 31, 32, 39B lie within or include other fields but the bounding regions are new (hence labelled 'HerMES' or VIDEO) and have been planned with the expectation of subsequent follow-up with the SCUBA-2 Cosmology Legacy Survey (Dunlop et al., in preparation), the *Spitzer* SERVS survey (Lacy & SERVS team 2009) and the VISTA-VIDEO survey (Bonfield, Jarvis & consortium 2010). The fields #29, 32 and 39B were jointly defined in coordination with VISTA-VIDEO who fixed the final field location.

APPENDIX B: MODELLING OF SPIRE DITHERING PATTERNS

SPIRE maps are built by scanning an array of bolometers across the sky in a raster with long scan legs each separated by a short step, $\theta_{\max}$ (e.g. $\theta_{\max} = 348$ arcsec for SPIRE 'Large Map' mode). The resulting hit rate or coverage of detector read-outs per sky bin is non-uniform (an effect which is exacerbated by dead or noisy bolometers). This non-uniform coverage can be improved by 'dithering', i.e. repeating scan with offsets. We have modelled this to try and optimize the dithering pattern.

Since we are interested in point sources, we can assume that the detector read-outs will be combined with a point source filter (e.g. Smith et al. 2011). The flux estimator for a source, $\hat{f}$ will be given by the

$$\hat{f} = \frac{\sum_i w_i d_i / P_i}{\sum_i w_i},$$

where d_i is the read-out of detector i, P_i is the point source profile for the source at detector i and w_i is a weighting. The optimal filter for isolated sources is $w_i = P_i^2/\sigma_i^2$, where σ_i is the noise of the detector i. The variance in this estimator is

$$V = \sigma_{\hat{f}}^2 = \frac{1}{\sum_i w_i^2} = \left(\sum_i \frac{P_i^2}{\sigma_i^2}\right)^{-1}. \tag{B1}$$

We can consider the two scan directions independently, so we need only model the coverage in one dimension. The sequential scan legs introduce a symmetry on the scale $\theta_{\max}$, so we project each bolometer position on to the range $0 < \theta_i < \theta_{\max}$ in the cross-scan direction. We then construct a one-dimensional variance profile $V(\theta)$ by analogy with equation (B1) setting P_i the point spread function $P(\theta - \theta_i)$. For simplicity, we set $w_i = 0$ for dead or noise bolometers and $\sigma_i = 1$ otherwise and used Gaussian beams with FWHM = 18.15/25.15/36.3 arcsec for the three bands.

We then defined a metric, M, to optimize dither patterns, on the understanding that we want to reduce the variation in variance. When considering the dither pattern for one band in isolation, we simply used the fractional variance of the variance

$$M^2 = \left\langle \sum \left(\frac{V - \bar{V}}{\bar{V}}\right)^2 \right\rangle,$$

where the sum is over the profile. As the SPIRE bolometers scan the sky simultaneously in all bands, any dithering scheme would apply to all bands. However, considering three bands simultaneously, there is no obvious metric (unless we considered sources of a particular colour); we did define an arbitrary metric $M^2 = M_{\rm PSW}^2 + M_{\rm PMW}^2 + M_{\rm PLW}^2$ but have restricted this discussion to the single bands independently.

The aim is to choose a dither pattern that minimizes M. If N independent scan maps with $N - 1$ dither positions are available, then the dither pattern is defined by $N - 1$ offsets $\Delta\theta$. We adopted four approaches: (a) optimization by brute-force search through $N - 1$ dimensional space (only attempted up to $N = 4$), (b) sequential optimization where we chose the best $\Delta\theta_i$ for each additional dither, i, given the $\Delta\theta$ found for the previous $i - 1$ dithers, (c) equal spacing $\Delta\theta_1 = \Delta\theta_2 = \cdots = \theta_{\max}/N$ and (d) random spacing with $\Delta\theta_i$ uniformly selected from $0 < \Delta\theta_i < \theta_{\max}$.

Downloaded from http://mnras.oxfordjournals.org/ at NASA Goddard Space Flight Ctr on July 14, 2014

For low values of $N \leq 4$ where both were calculated, we found that the brute-force optimization (a) agreed reasonably well with the sequential optimization (b). We found that the equal spacing (c) performed similarly to the sequential optimization at low N and typically better at high N ($\gtrsim 10$), except at specific N (e.g. $N = 15$ for PSW and $\theta_{\max} = 348$ arcsec) when the projected bolometer spacing were in phase. Random offsets (d) were invariably worst. The raw variation with no dithers ($N = 1$) was 12, 15 and 10 per cent for PSW, PMW and PLW, respectively; this declined rapidly to about 3 per cent by $N = 3$ and was <1 per cent for $N > 16$.

A penalty for dithering with these large steps is that the ramp down in coverage at the edges of the map is more gradual, i.e. less area at the full coverage with more area at low coverage. When designing offsets in both scan directions, we chose pairs of offsets tracing a square to reduce the impact of this ramp-down and this strategy is included in the SPIRE Observers' Manual.

This paper has been typeset from a TEX/LATEX file prepared by the author.

Downloaded from http://mnras.oxfordjournals.org/ at NASA Goddard Space Flight Ctr on July 14, 2014